NEUROSCIENCE

A robust expression system reveals distinct gating mechanisms and calmodulin regulation of $Na_V1.9$ channels

Margaux Theys[1], Jolien De Waele[1], Sharang Garud[2], Katrien Willegems[2], Filip Van Petegem[2], Frank Bosmans[1,3]*

$Na_V1.9$ is a voltage-gated Na^+ channel subtype with unique gating properties that are poorly understood, partly due to the lack of reliable heterologous expression systems. Here, we present a transient expression protocol that produces robust mouse $Na_V1.9$ currents, enabling direct electrophysiological comparisons with native dorsal root ganglion neurons. To further understand the low current density observed in human $Na_V1.9$, we created chimeras with $Na_V1.5$ and identified a role for the C-tail—specifically the IQ motif and EF-hand—in regulating current densities, likely due to a weak affinity for calmodulin. Isothermal titration calorimetry experiments indicated that, unlike other Na_V channel subtypes, calmodulin binding to the C-tail is likely too weak to occur under physiological conditions. Markedly, the pre-IQ region did not influence channel expression but was responsible for conferring the characteristic depolarized voltage dependency of inactivation of $Na_V1.9$. Our findings provide insights into the unique gating mechanisms of $Na_V1.9$ and demonstrate the robustness of this platform for structure-function studies.

INTRODUCTION

Among the nine voltage-gated Na^+ (Na_V) channel subtypes ($Na_V1.1$ to $Na_V1.9$) identified in mammals (*1*), $Na_V1.9$ has proven to be particularly challenging to study (*2*–*6*). For example, while Na_V channels are typically associated with generating and propagating action potentials, the slow activation kinetics of $Na_V1.9$ likely preclude it from substantially contributing to the action potential upstroke (*7*). Also, its slow inactivation kinetics lead to persistent Na^+ currents near the resting membrane potential (*8*, *9*). Such currents can amplify and sustain depolarizations, thereby modulating neuronal excitability without directly governing action potentials (*10*). A thorough mechanistic explanation for the unique gating properties of $Na_V1.9$ is lacking, mainly due to challenges associated with heterologous expression (*11*–*16*). Unlike other Na_V channel subtypes, transient expression of $Na_V1.9$ in heterologous systems yields minimal or no ionic currents, usually inadequate for patch-clamp electrophysiology analysis. As such, most $Na_V1.9$ gating data are derived from experiments with isolated dorsal root ganglion (DRG) neurons, where $Na_V1.9$ is endogenously expressed alongside other Na_V channel subtypes (*9*, *17*–*19*). $Na_V1.8$ and $Na_V1.9$ are tetrodotoxin (TTX) resistant, allowing their study in DRG by eliminating TTX-sensitive currents (*20*). The use of specific $Na_V1.8$ inhibitors can further facilitate the isolation of $Na_V1.9$-mediated currents (*21*, *22*). Alternatively, intracellular fluoride administered via the patch pipette causes a pronounced hyperpolarizing shift in $Na_V1.9$ activation voltage, creating a window of membrane potentials where $Na_V1.9$ currents can be observed with minimal interference from $Na_V1.8$ (*16*, *23*). In $Na_V1.8^{-/-}$ mice, the $Na_V1.9$ function can be examined in combination with only TTX (*19*, *20*). DRG approaches, however, are labor-intensive and complicate studies requiring channel manipulations such as mutagenesis.

To address these limitations, developing an efficient protocol for transient heterologous expression of $Na_V1.9$ would be advantageous, especially for advancing detailed gating and structure-function studies. Our protocol is not only sufficient for producing robust currents but is also easy to carry out, requiring no extensive experience or use of challenging techniques, making it accessible for a wide range of research labs. Although progress has been made, the reliability of current methods is limited. Reported strategies include low-temperature incubation (28° to 30°C) (*13*, *14*, *24*–*26*), cotransfection of the channel with auxiliary β_1 and β_2 subunits (*13*), and using the ND7/23 neuronal cell line (*24*–*26*), derived from mouse neuroblastoma and rat DRG cells. An alternative approach involves the use of chimeric channels, incorporating the C-tail of rat $Na_V1.4$ (*12*) or human $Na_V1.7$ ($hNa_V1.7$) (*14*) to enhance ionic currents of the resulting $Na_V1.9$ variant, albeit via an unclear working mechanism. Last, increased current amplitudes can be obtained by manipulating voltage protocols or adding fluoride and/or guanosine 5′-*O*-(3′-thiotriphosphate) (GTP-γ-S) to the intracellular solution (*18*, *23*, *25*, *27*–*30*). However, applying these compounds may not be practical in all contexts, such as when examining interactions between $Na_V1.9$ and G protein–coupled receptors (*3*, *20*, *25*, *31*). Notably, three $Na_V1.9$ stable cell lines have been produced, but neither has been replicated, is freely available for academic use, nor is conducive to structure-function studies (*13*, *25*, *32*).

Here, we report the development of an alternative method capable of reliably generating robust $Na_V1.9$ currents in a heterologous expression system after transient transfection. Our strategy allowed us to consistently express mouse $Na_V1.9$ ($mNa_V1.9$), record ionic currents of wild-type and mutant channels, and compare our findings to mouse DRG (mDRG). Next, we investigated possible reasons for the low current density of $hNa_V1.9$ when applying this approach by using chimeras with $hNa_V1.5$, our reference channel that expresses abundantly in many cell types (*33*, *34*) . As a result, we identified a functional role for the cytosolic C-tail in governing $hNa_V1.9$ expression

[1]Molecular Physiology and Neurophysics group, Department of Basic and Applied Medical Sciences, Faculty of Medicine and Health Sciences, University of Ghent, Ghent 9000, Belgium. [2]Department of Biochemistry and Molecular Biology, Life Sciences Centre, University of British Columbia, Vancouver, BC, Canada. [3]Experimental Pharmacology group (EFAR), Department of Pharmaceutical Sciences, Faculty of Medicine and Pharmaceutical Sciences, Vrije Universiteit Brussel, Brussels 1050, Belgium.
*Corresponding author. Email: frank.bosmans@vub.be

and function. In virtually all Na_V channel subtypes, this region binds calmodulin (CaM) under both Ca^{2+}-free and Ca^{2+}-loaded conditions (*35*–*39*). Mutations in the C-tail have been shown to affect the channel function, including inactivation (*40*–*43*), and disruption of CaM binding can increase persistent Na^+ currents (*42*), a prominent feature of $Na_V1.9$. Markedly, the amino acid sequence of the $Na_V1.9$ C-tail differs substantially from other Na_V channel subtypes and the subsequent impact on CaM binding remains unclear. Our combined findings suggest a low affinity of the $Na_V1.9$ C-tail for CaM with differential effects of the EF-hand, the pre-IQ region, and the IQ domain on channel expression levels and gating.

RESULTS

Heterologous $mNa_V1.9$ expression and functional characterization

To attain robust $Na_V1.9$ ionic currents, multiple reported approaches to enhance the functional expression of ion channels, including $Na_V1.9$, were evaluated. In addition, we applied various methodologies used to augment the expression or function of a range of proteins to $Na_V1.9$ (table S1). However, all these efforts failed to produce reliable $Na_V1.9$ currents, propelling us to develop a more effective heterologous expression protocol. Ultimately, we achieved robust and reproducible $Na_V1.9$ expression by using a multifaceted procedure (see Materials and Methods for additional details). First, $Na_V1.9$-encoding cDNA was cloned into the pcDNA3.4 vector, which includes the woodchuck hepatitis posttranscriptional regulatory element to boost transgene expression. Second, ND7/23 cells were transiently transfected with this construct along with β_1 and β_2 subunits and incubated for 48 hours. The initial 24 hours of incubation was at 37°C, followed by 24 hours at 28°C. Third, fluoride was added to the intracellular solution for electrophysiological recordings and allowed to diffuse for up to 7 min after membrane rupture before recordings commenced. This protocol was executed with $mNa_V1.9$ and $hNa_V1.9$, whereas $hNa_V1.5$ was used as a reference channel in combination with a standard transfection protocol. When applying these steps, we consistently observed $mNa_V1.9$-mediated currents in more than 80% of transfected cells (Fig. 1A and fig. S2A). Similar to previous reports (*20*, *23*, *30*, *44*), gating parameters of $mNa_V1.9$ (Fig. 1B) changed with time after membrane rupture, underscoring the need to standardize the timing of these experiments. Current density increased from 14.5 ± 2.2 pA/pF at 5 min to 24.2 ± 3 pA/pF at 7 min postrupture ($P = 0.0001$) (Fig. 1C and Table 1). The half-maximal activation voltage (V_{50}) hyperpolarized by ~4.6 mV per minute from −41.5 ± 1.5 mV at 5 min to −50.6 ± 1.2 mV at 7 min (Fig. 1D and Table 1). The slope factor (k) decreased from 10.8 ± 1 at 5 min to 7.6 ± 0.5 at 7 min. Persistent current (I_p) percentage measured at 100 ms after channel opening and normalized to peak current was 12% lower at 5 min versus 7 min. I_p at 500 ms, time to peak (TTP), and time constant (τ) of fast inactivation did not change significantly during this 2-min time course (Fig. 1, E to G, and Table 1). Similar observations were made with $hNa_V1.5$, albeit less pronounced (Fig. 1, A and B, fig. S3, and table S2). The V_{50} of activation hyperpolarized at a rate of 1.8 mV/min from 5 to 7 min, and current density increased from 263.7 ± 70.3 to 284 ± 73 pA/pF.

Earlier work had shown that $Na_V1.9$ in DRG exposed to intracellular GTP-γ-S, a hydrolysis-resistant guanosine 5′-triphosphate analog, exhibited increased current density, slowing of inactivation, and a depolarizing shift in the voltage dependency of inactivation

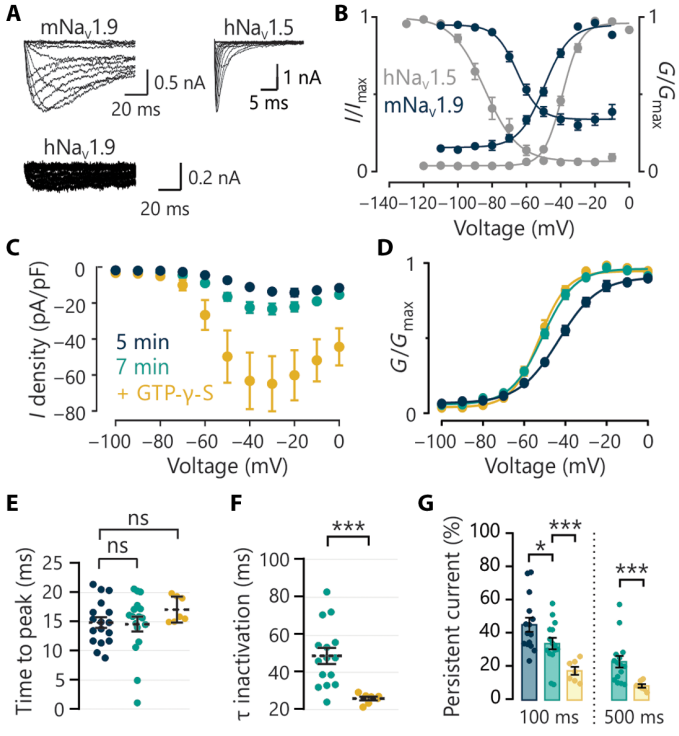

Fig. 1. Characterization of $mNa_V1.9$ currents in ND7/23 cells. (**A**) Trace and (**B**) activation voltage (*G-V*) and channel availability (*I-V*) curve comparison between $mNa_V1.9$ (blue) and $hNa_V1.5$ (gray) highlight typical features of $Na_V1.9$ gating including large persistent currents, hyperpolarized activation voltage, depolarized voltage dependency of inactivation, and slow kinetics of activation as well as inactivation. $hNa_V1.9$ currents were too small for accurate analysis (A). $mNa_V1.9$ currents were recorded in ND7/23 cells and $hNa_V1.5$ currents in HEK293T cells. $mNa_V1.9$ channel activation over time [5 min (dark blue) versus 7 min (teal)] and in the presence of 200 μM GTP-γ-S (yellow), illustrating (**C**) current density augmentation and (**D**) channel opening at more negative voltages. (**E**) Time to peak is not significantly different under measured conditions. ns, not significant. (**F**) GTP-γ-S accelerates inactivation kinetics (τ) and (**G**) reduces persistent currents. Because a time frame of 100 ms was insufficient to calculate the time constant (τ) of inactivation, recordings at the 7-min time point were used where the test pulse duration was 500 ms. $^*P < 0.05$ and $^{***}P < 0.001$.

but no change in activation voltage (*25*, *29*, *30*). In our $mNa_V1.9$ expression system, the addition of 200 μM GTP-γ-S to the intracellular solution also altered channel activity (Fig. 1, C to G, and Table 1). Current density was about 4.5 times higher in recordings with GTP-γ-S (65.8 ± 15.8 pA/pF), and the V_{50} of activation voltage shifted ~11 mV to hyperpolarized voltages (−52.2 ± 1.4 mV), close to the V_{50} observed at 7 min without GTP-γ-S. The slope of the activation curve decreased to 6.7 ± 0.4. TTP did not change significantly. In contrast to the over-time comparisons, GTP-γ-S significantly fastened inactivation kinetics and reduced persistent currents measured at 100 and 500 ms.

Next, we compared a subset of biophysical parameters of $mNa_V1.9$ currents recorded from ND7/23 cells to mouse DRG and observed notable differences (Fig. 2, A to D, and Table 1). First, TTP was 3.5 times longer in DRG with a value of 37.5 ± 4.3 ms versus 10.3 ± 0.9 ms in ND7/23 cells (Fig. 2B). Second, persistent currents were 21% larger in DRG at the 100-ms time point (Fig. 2D). Third, while the voltage dependency of activation did not differ significantly in DRG (−40.5 ± 1.73 mV), the V_{50} of the channel availability curve (i.e.,

Table 1. Characterization of mNa$_V$1.9 currents (top) and relevant parameters of chimeras (bottom). Top: parameter and *P* value summary of heterologous mNa$_V$1.9 currents over time (5 min versus 7 min) without and with 200 μM GTP-γ-S and comparison to native currents in primary DRG neurons. All *P* values were calculated using pairwise comparisons to mNa$_V$1.9 at 5 min or at 7 min for inactivation parameters. Voltage protocols for calculation of the voltage dependency of inactivation after 7 min are reported in the text and fig. S1. Because inactivation kinetics were too slow to reliably measure a time constant [τ (ms)] over 100 ms, data in this table were derived from the 500-ms prepulse in the voltage dependency of inactivation protocol, as was the I_p at 500 ms. Timing was the same for DRG parameters. Data are presented as the means ± SEM. Voltage protocols for calculating the voltage dependency of inactivation were ran at 7 min. Bottom: The time constant of inactivation (τ) was calculated over a 50-ms pulse in all constructs except for Na$_V$1.9-1.5Ctail where the pulse duration was 100 ms. *I* dens, current density (pA/pF); V_{50}, half-maximal voltage (mV); *k*, slope factor; TTP, time to peak (ms); act, activation; inact, inactivation; I_p, persistent current (%); ND, not determined; **P* < 0.05, ***P* < 0.01, ****P* < 0.001, *****P* < 0.0001.

	mNa$_V$1.9 (5 min)	mNa$_V$1.9 (7 min)		mNa$_V$1.9 + GTP-γ-S		mNa$_V$1.9 from DRG	
	mean ± SEM (*n*)	mean ± SEM (*n*)	*P* value	mean ± SEM (*n*)	*P* value	mean ± SEM (*n*)	*P* value
I dens	14.5 ± 2.2 (17)	24.2 ± 3 (17)	1.5×10^{-5} (****)	65.8 ± 15.8 (7)	4.1×10^{-5} (****)	43.7 ± 10 (30)	1.0×10^{-4} (***)
V_{50} act	−41.5 ± 1.5 (17)	−50.6 ± 1.2 (17)	1.5×10^{-5} (****)	−52.2 ± 1.4 (7)	5.0×10^{-5} (****)	−38.5 ± 1.8 (25)	0.21 (ns)
k act	10.8 ± 1.1 (17)	7.6 ± 0.5 (17)	0.0026 (**)	6.7 ± 0.4 (7)	0.001 (**)	6.2 ± 0.6 (25)	4.2×10^{-5} (****)
V_{50} inact	ND	−63.9 ± 1.2 (13)		ND		−40.5 ± 1.7 (19)	4.3×10^{-12} (****)
k inact	ND	−6.5 ± 0.5 (13)		ND		−8.1 ± 0.6 (19)	0.057 (ns)
TTP	10.3 ± 0.91 (17)	10.6 ± 1.3 (17)	0.96 (ns)	8.1 ± 0.8 (7)	0.14 (ns)	37.5 ± 4.3 (24)	1.9×10^{-6} (****)
τ inact	ND	48.2 ± 4.3 (15)		25.5 ± 1 (7)	1.1×10^{-4} (***)	108.1 ± 19 (21)	0.17 (ns)
I_p 100 ms	0.45 ± 0.04 (15)	0.33 ± 0.03 (15)	0.024 (*)	0.17 ± 0.02 (7)	8.7×10^{-4} (***)	0.66 ± 0.06 (21)	0.008 (**)
I_p 500 ms	0.23 ± 0.04 (15)	ND		0.08 ± 0.01 (7)	5.3×10^{-4} (***)	0.26 ± 0.04 (21)	0.43 (ns)

	Na$_V$1.5	Na$_V$1.9-1.5Ctail	Na$_V$1.5-1.9Ctail	Na$_V$1.5-1.9IQ	Na$_V$1.5-1.9preIQ-EF	Na$_V$1.5-1.9preIQ
I dens	202.7 ± 25.1 (20)	30.1 ± 3.7 (12)	72.6 ± 9.5 (18)	126.4 ± 13.6 (12)	102.1 ± 12.1 (18)	−204.4 ± 39.7 (16)
V_{50} act	−33 ± 1.2 (14)	−61.4 ± 1.2 (12)	−28.1 ± 1.1 (18)	−30.3 ± 1.8 (9)	−24.5 ± 1.0 (18)	−29.4 ± 0.9 (11)
k act	8.0 ± 0.4 (14)	9.7 ± 0.6 (12)	7.2 ± 0.4 (18)	8.0 ± 0.5 (9)	9.8 ± 0.5 (18)	7.0 ± 0.4 (11)
V_{50} inact	−79.7 ± 2.3 (14)	−90.8 ± 1.4 (9)	−57.5 ± 1.9 (14)	−86.1 ± 3.3 (9)	−60.3 ± 2.0 (17)	−59.6 ± 4.3 (8)
k inact	−8.1 ± 0.5 (14)	−8.1 ± 0.5 (9)	−6.9 ± 0.6 (14)	−9.9 ± 0.5 (9)	−6.2 ± 0.3 (17)	−7.0 ± 0.6 (8)
TTP	1.0 ± 0.04 (14)	6.4 ± 0.8 (12)	1.1 ± 0.1 (17)	1.2 ± 0.1 (9)	0.8 ± 0.04 (18)	1.3 ± 0.1 (12)
τ inact	1.9 ± 0.4 (14)	29.8 ± 3.9 (12)	1.9 ± 0.1 (17)	3.1 ± 0.6 (9)	1.4 ± 0.2 (18)	4.2 ± 0.4 (11)
I_p 50 ms	0.07 ± 0.02 (14)	0.4 ± 0.04 (9)	0.08 ± 0.01 (18)	0.1 ± 0.01 (6)	0.07 ± 0.02 (11)	0.05 ± 0.02 (5)

voltage dependency of inactivation) was shifted in DRG to depolarized potentials by ~23 mV to −40.5 ± 1.73 mV (Fig. 2C and Table 1). These findings align with our expectations, as it is well established that ion channels can exhibit different gating behaviors depending on the expression system used (*1*). This variation can be attributed to several key factors such as (i) the presence of auxiliary subunits, (ii) posttranslational modifications, (iii) the cellular environment including factors like membrane composition and signaling pathways, and (iv) different levels of endogenous ion channel expression.

In contrast to mNa$_V$1.9, transfection of the human ortholog *SCN11A* (hNa$_V$1.9) using our methodology did not produce sufficient expression for detailed electrophysiological analysis (Fig. 1A and fig. S2B). Although some cells exhibited small persistent inward currents, these could not be definitively identified as mediated by hNa$_V$1.9 because of the presence of endogenous currents in untransfected ND7/23 cells. These currents have similar amplitudes and trace morphologies but are likely generated by Ca$_V$ channels, as ND7/23 cells are known to express these in their differentiated state (*45*, *46*). We next concentrated on hNa$_V$1.9, exploring potential causes for its expression failure in ND7/23 cells following transient transfection and assessing methods to enhance current amplitudes.

Heterologous expression and functional properties of hNa$_V$1.9-based chimeras

To examine possible causes of low hNa$_V$1.9 expression, chimeric hNa$_V$1.9-hNa$_V$1.5 constructs were generated. Distinct regions based on the four-domain architecture of Na$_V$ channels [DI to DIV, each consisting of six transmembrane segments, S1 to S6 (*44*, *45*, *47*)]

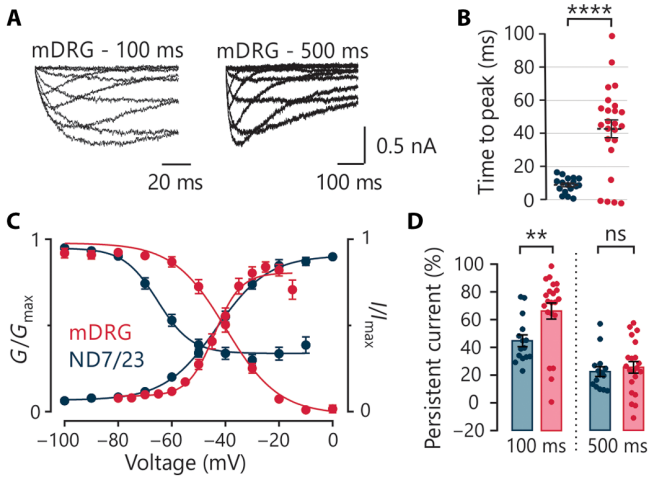

Fig. 2. Comparison of mNa$_V$1.9 gating properties in ND7/23 cells to DRG neurons. Endogenous mNa$_V$1.9 currents in DRG neurons (red) show markedly slower kinetics compared to those observed in ND7/23 cells (blue). This is illustrated by (**A**) the Na$_V$1.9-current trace recorded from DRG on two different timescales (left: first 100-ms pulse duration; right: 500-ms pulse duration), (**B**) peak currents being reached up to four times slower, and (D) slowed inactivation as indicated by a larger persistent current component at 100 ms but not 500 ms. mDRG, mouse DRG. In addition, (**C**) the channel availability curve of currents recorded from DRG was depolarized by ~20 mV compared to mNa$_V$1.9 currents measured in ND7/23 cells. Although the offset of the channel availability curve from heterologous mNa$_V$1.9 seems to suggest that persistent currents were larger in ND7/23 cells compared to DRG, this was not reflected in absolute measurements of persistent current at peak voltage (**D**). Most likely, this discrepancy is due to the smaller size of heterologous currents and the presence of other endogenous currents in ND7/23 cells, especially at higher voltages (fig. S2). DRG data were obtained from two biological replicates. $^{**}P < 0.01$ and $^{****}P < 0.0001$.

were demarcated with unique restriction sites in both hNa$_V$1.5 and hNa$_V$1.9, with transition sites located in conserved sections in the intracellular loops between domains. By substituting hNa$_V$1.9 regions with corresponding amino acid sequences from hNa$_V$1.5, we generated five chimeras: hNa$_V$1.9-1.5DI, hNa$_V$1.9-1.5DII, hNa$_V$1.9-1.5DIII, hNa$_V$1.9-1.5DIV, and a separate hNa$_V$1.9-1.5Ctail construct. Transfection was performed according to the protocol described for mNa$_V$1.9. Successful transfection was confirmed with immunofluorescence staining against the attached N-terminal sfEGFP (superfolder enhanced green fluorescent protein) tag that was included in all hNa$_V$1.9-based constructs (fig. S4). These chimeras were inserted into the common pcDNA3.1 vector as opposed to the pcDNA3.4 plasmid.

Of all constructs, only hNa$_V$1.9-1.5DI and hNa$_V$1.9-1.5Ctail resulted in a discernible improvement of current density compared to wild-type hNa$_V$1.9 (Fig. 3A). Notably, when low-temperature incubation and supplementary β subunits were omitted from the protocol, Na^+ currents were undetectable in all constructs. In the case of hNa$_V$1.9-1.5DI, currents could be characterized from only 3 of 52 cells recorded (5.8%). The sample size was therefore too low for reliable electrophysiological characterization. However, kinetics and gating parameters from resulting currents resembled those of Na$_V$1.5 rather than Na$_V$1.9 (Fig. 3B). In contrast, the hNa$_V$1.9-1.5Ctail chimera yielded an average current density of 30.14 ± 3.7 pA/pF, three times higher than the average current density observed after transfection of hNa$_V$1.9 [8.98 ± 0.89 pA/pF (*13*), $P < 0.001$] and about twice the size of wild-type mNa$_V$1.9 in pcDNA3.4 ($P < 0.001$) (Fig. 3A and Table 1). Overall, the trace morphology of this chimera resembled that of mNa$_V$1.9 (Fig. 3B), although kinetics were significantly faster and the persistent component was reduced by half. Significant shifts in voltage dependency were also detected: The V_{50} of activation voltage was hyperpolarized by 20 mV to −61.4 ± 1.2 mV ($P < 0.0001$), and the V_{50} of the channel availability curve was hyperpolarized by ~27 mV to −90.8 ± 1.4 mV ($P < 0.0001$) (Fig. 3, C to F). As observed with Na$_V$1.9, Na^+ influx through the hNa$_V$1.9-1.5Ctail chimera changed over time after membrane rupture (fig. S5 and table S4): Current density increased significantly, and the V_{50} of activation voltage hyperpolarized by 2.3 mV/min. The magnitude of this effect was intermediate between that observed for mNa$_V$1.9 and hNa$_V$1.5. Contrary to mNa$_V$1.9, the TTP parameter slowed significantly between 3 and 7 min, whereas I_p remained constant.

To further examine these observations, we made a reverse chimera based on hNa$_V$1.5, replacing its C-tail with the corresponding region of hNa$_V$1.9. The resulting construct was transfected into commonly used human embryonic kidney (HEK) 293T cells, and current recordings were compared to those obtained from hNa$_V$1.5-expressing cells. Introduction of the hNa$_V$1.9 C-tail reduced current density to less than half of the original hNa$_V$1.5 levels ($P < 0.0001$) (Fig. 4A and Table 1). This decrease is most likely driven by a hampered translation or trafficking process rather than transcription, considering that quantitative polymerase chain reaction (PCR) yielded no notable differences in mRNA levels (fig. S6). Electrophysiological examination revealed no changes in activation or inactivation kinetics (Fig. 5) and a modest but significant rightward shift in the conductance-voltage relationship of 5 mV compared to hNa$_V$1.5 ($P = 0.023$) with no impact on the slope factor ($P = 0.7$) (Figs. 4, B to D, and 6). In contrast, a pronounced 22-mV depolarization of the channel availability curve into the direction of mNa$_V$1.9 (Fig. 5) was observed ($P < 0.0001$), a result that prompted further study.

Investigation of CaM binding to the C-tail of hNa$_V$1.9

We postulated that an explanation for the pronounced shift in channel availability could stem from a different binding affinity of CaM for the IQ motif in the proximal C-tail of hNa$_V$1.9 relative to other Na$_V$ channel subtypes (*46*, *48*–*50*). Binding of CaM to the IQ domain has been shown to affect the inactivation process of hNa$_V$1.5, our reference channel (*42*). The ability of the hNa$_V$1.9 IQ domain to interact with CaM in the presence and absence of Ca^{2+} was assessed with isothermal titration calorimetry (ITC). Using this method to measure thermodynamic parameters of biomolecular interactions, we found that the binding of apoCaM (Ca^{2+}-free CaM) to the hNa$_V$1.9 IQ domain was weak, with an affinity (K_d) value of ~37 μM (Fig. 7 and table S5). Similar to other Na$_V$ channel isoforms, the binding in the presence of Ca^{2+} was even weaker (*39*, *51*) and yielded unstable fits and an estimated K_d value of ~480 μM. However, this value is at least two orders of magnitude weaker than reported for hNa$_V$1.5 or other subtypes (*39*, *51*). To test whether this low affinity might prompt the observed shift in channel availability, we designed an hNa$_V$1.5 chimera harboring the IQ domain of hNa$_V$1.9 (hNa$_V$1.5-1.9IQ). The current density of this construct decreased from 202.74 ± 25.05 to 126.36 ± 13.59 pA/pF (Fig. 4A and Table 1), which was not significant ($P = 0.3$) after post hoc corrections because of typical variability observed in current density measurements. However, channel availability (Fig. 5 and Table 1) did not differ significantly from wild-type hNa$_V$1.5 ($P = 0.41$). No changes in other gating

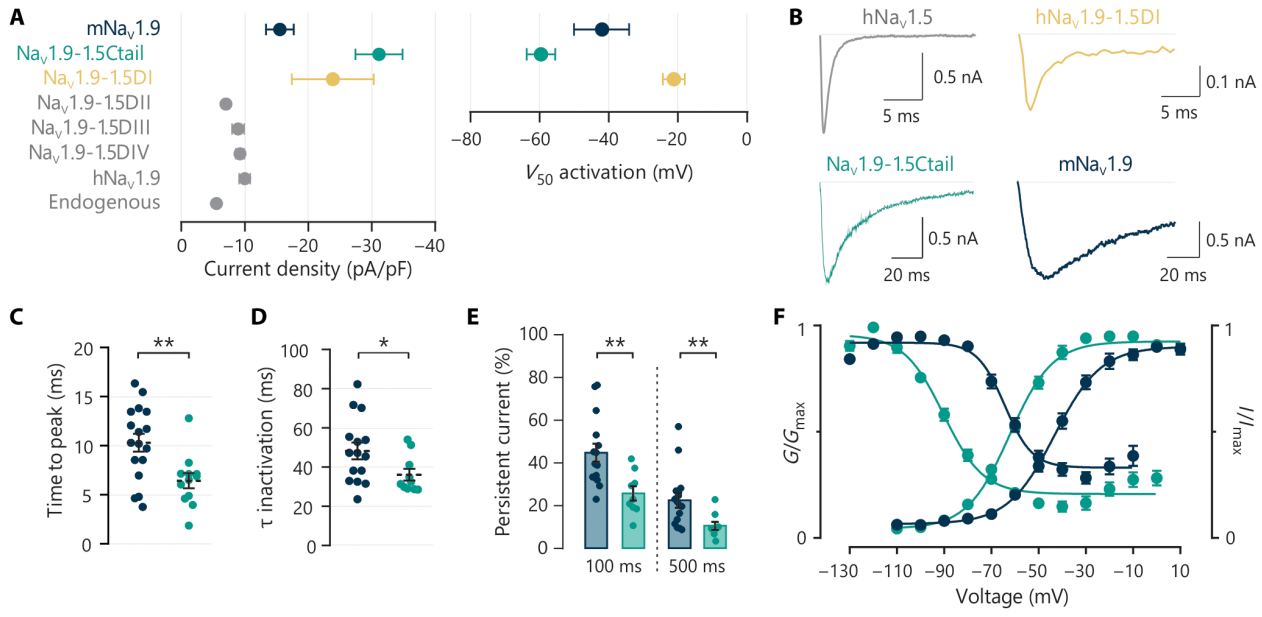

Fig. 3. Gating characterization of hNaV1.9-based chimeras in ND7/23 cells. (**A**) Left: Only transient transfection of mNaV1.9 (dark blue) and the hNaV1.9-1.5Ctail (teal) construct generated measurable currents. hNaV1.9-1.5DI currents (yellow) were observed in 3 of 52 cells. Right: Half-maximal activation voltage of both of these NaV1.9-based chimeras revealed sizable shifts. (**B**) Comparison of traces at peak voltage illustrates the resemblance of hNaV1.9-1.5DI to hNaV1.5 (gray) and of hNaV1.9-1.5Ctail to mNaV1.9. However, kinetics of (**C**) activation as well as (**D**) inactivation of the hNaV1.9-1.5Ctail construct are faster, and (**E**) persistent current fraction is lower. (**F**) Both activation voltage and channel availability curves of hNaV1.9-1.5Ctail are hyperpolarized compared to mNaV1.9. *$P < 0.05$ and **$P < 0.01$.

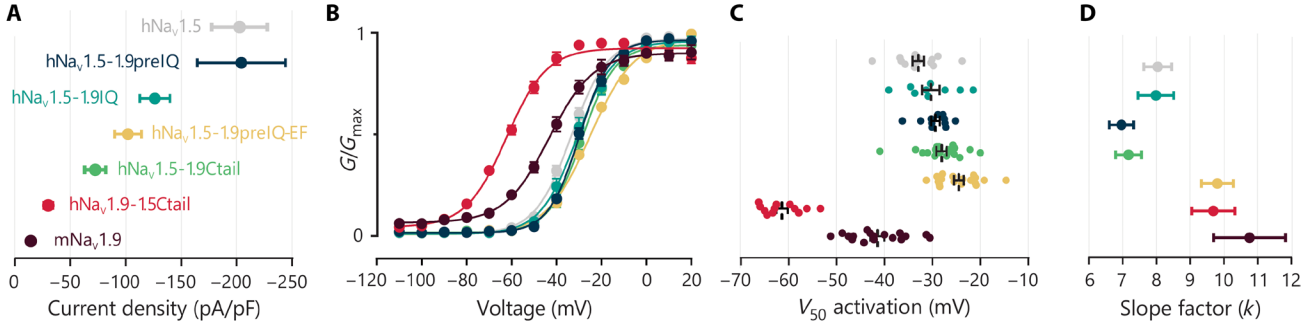

Fig. 4. Current density and voltage dependency of activation of hNaV1.5-based C-tail chimeras. (**A**) Current density comparison of all hNaV1.5-1.9 chimeras (HEK293T), hNaV1.5 (HEK293T), hNaV1.9-1.5Ctail (ND7/23), and mNaV1.9 (ND7/23). (**B**) Conductance (*G*)-voltage (*V*) relationships of all constructs. (**C**) Individual half-maximal activation voltage and (**D**) slope factors calculated separately for each cell.

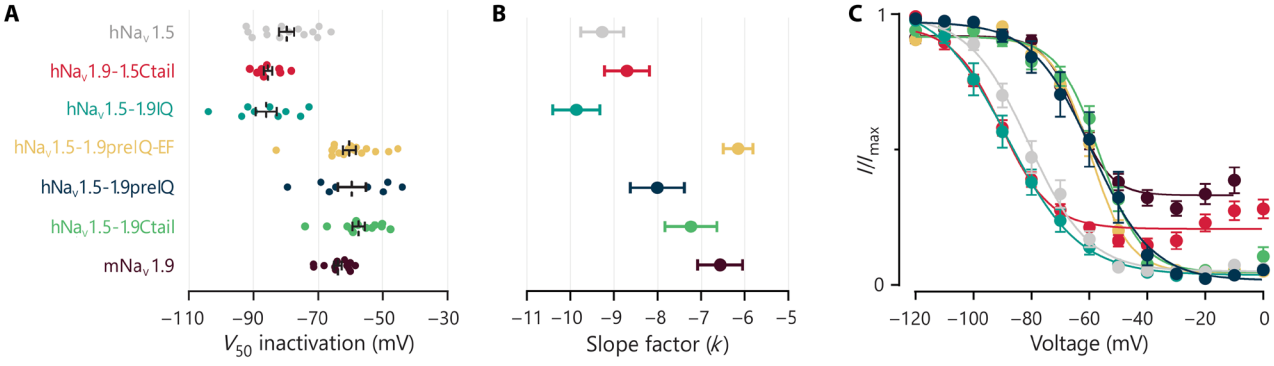

Fig. 5. Voltage dependency of inactivation of hNaV1.5-based C-tail chimeras. (**A**) Half-maximal inactivation voltage and (**B**) slope factors of channel availability curves calculated per cell for all hNaV1.5-1.9 chimeras (HEK293T), hNaV1.5 (HEK293T), hNaV1.9-1.5Ctail (ND7/23), and mNaV1.9 (ND7/23). (**C**) Overview of mean channel availability curves for all constructs.

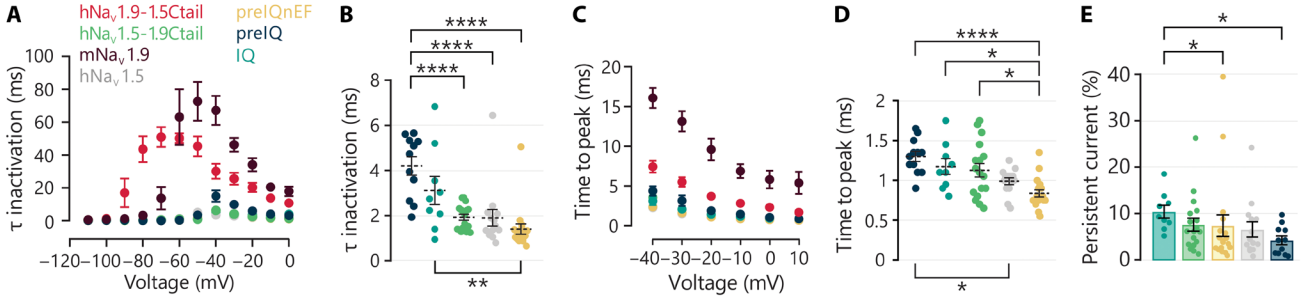

Fig. 6. Comparison of activation and inactivation kinetics of all tested chimeras. (**A**) The time constant of inactivation (τ) and (**C**) time to peak in the function of pulse voltage for all constructs illustrate differences between $Na_V1.9$- and $hNa_V1.5$-based constructs. (**B**) Detailed comparison of inactivation time constants at voltages at which peak current was reached (−40 to −10 mV; see Materials and Methods) between $hNa_V1.5$-based constructs. Although the increase in $hNa_V1.5$-1.9IQ compared to $hNa_V1.5$ did not reach statistical significance after post hoc corrections ($P = 0.11$), the difference was significant compared to $Na_V1.5$-1.9preIQ-EF (yellow). (**D**) Similar analysis of activation parameters also indicated slower kinetics for $hNa_V1.5$-1.9preIQ, while $hNa_V1.5$-1.9preIQ-EF tended to be faster than other constructs. The difference between $hNa_V1.5$-1.9preIQ-EF and $hNa_V1.5$ was, however, not significant ($P = 0.19$). (**E**) A small but significant increase in persistent current was found for the $hNa_V1.5$-1.9IQ construct compared to some of the other constructs, although the difference fell just below the significance criterion for the comparison with $hNa_V1.5$ ($P = 0.078$). All *P* values can be found in tables S6 to S13. *$P < 0.05$, **$P < 0.01$, and ****$P < 0.0001$.

parameters were observed (tables S7 to S10). Because determinants for CaM binding are also found in regions preceding the IQ domain (*39*, *51*), we next tested—with ITC—a $Na_V1.9$ C-tail construct encompassing the EF-hand, pre-IQ, and IQ domain for CaM binding. We observed that the binding of apoCaM appeared significantly weaker compared to just the IQ domain, with a K_d value of ~214 μM (Fig. 7 and table S5). The binding of Ca^{2+}/CaM to the extended C-tail construct improved about sevenfold compared to just the IQ domain, with a K_d value of ~70 μM. One caveat here is that we noted a low ΔH value for this interaction, which may affect the accuracy of the extrapolated affinity value.

Propelled by these data, we next evaluated the impact of the pre-IQ and EF-hand region on channel availability using two additional $hNa_V1.5$ chimeras harboring either the $hNa_V1.9$ pre-IQ ($hNa_V1.5$-1.9preIQ) or pre-IQ and EF-hand ($hNa_V1.5$-1.9preIQ-EF) (Figs. 4 to 6 and Table 1). In contrast to $hNa_V1.5$-1.9IQ, patch-clamp recordings demonstrated a significant ~20-mV depolarization of channel availability in both of these constructs ($P < 0.0001$), driving it in the direction of $mNa_V1.9$ (Fig. 5 and Table 1). The V_{50} of channel availability did not differ significantly between the $hNa_V1.5$-1.9preIQ-EF and $hNa_V1.5$-1.9preIQ constructs ($P = 0.85$), indicating an unexpected role of the pre-IQ motif in regulating channel availability. In addition, the current density of the $hNa_V1.5$-1.9preIQ-EF construct was significantly lower (102.14 ± 12.07 pA/pF) compared to that of the $hNa_V1.5$-1.9preIQ construct (204.41 ± 39.65 pA/pF), which closely resembled that of wild-type $hNa_V1.5$ (Fig. 4A and Table 1). This suggests that the pre-IQ motif plays a distinct role in modulating channel availability. Although less pronounced, changes in other gating parameters including the voltage dependency of activation, kinetics, and persistent currents were also observed and are summarized in Fig. 6, Table 1, and tables S6 to S13.

Application of the ND7/23 expression system to pathogenic $Na_V1.9$ mutations

We sought to extend the utility of the $Na_V1.9$ heterologous expression system by investigating two previously characterized mutations, $mNa_V1.9^{p.L799P}$ and its human ortholog $hNa_V1.9^{p.L811P}$, associated with loss of pain and chronic itch (*52*, *53*). Both mutations induced a gain-of-function phenotype in DRG neurons by shifting voltage-dependent activation to more hyperpolarized potentials and enhancing persistent Na^+ currents. Using our methodology in ND7/23 cells, $mNa_V1.9^{p.L799P}$ caused a ~25-mV leftward shift in half-maximal activation voltage to −66.1 ± 3 mV ($P < 0.0001$) and significantly decelerated inactivation, with currents persisting to 56% of their original size after 500 ms compared to 23% in the wild-type channel ($P < 0.0001$) (Fig. 8 and table S14). Channel activation was also markedly slower, with TTP tripling to 10.3 ± 0.9 ms ($P < 0.001$). Although the voltage dependency of inactivation did not shift significantly, we observed a distinct decline in the slope of the curve from −6.5 ± 0.5 to −22.2 ± 4.6 ($P = 0.01$).

Because $hNa_V1.9$-mediated currents have proven more challenging to record with the proposed methodology, the p.L811P mutation was studied against the background of the $hNa_V1.9$-1.5Ctail construct. $hNa_V1.9$-1.5Ctail$^{p.L811P}$ currents demonstrated a leftward shift in half-maximal activation voltage similar to $mNa_V1.9^{p.L799P}$ (~25 mV, $P < 0.0001$) (Fig. 8 and table S15). The voltage dependency of activation was already considerably shifted in the $hNa_V1.9$-1.5Ctail construct versus $mNa_V1.9$, resulting in channel opening at voltages as low as −100 mV. As expected, kinetics of activation (32.8 ± 7.7 ms) and inactivation ($I_p = 43\%$ at 500 ms) were approximately threefold slower ($P < 0.0001$). The presence of large, persistent currents at low voltages complicated the calculation of the channel availability curve because of incomplete inactivation before the end of the 500-ms prepulse. As a result, currents measured during the subsequent depolarizing pulse are a combination of the opening of noninactivated channels and residual persistent currents, with the latter beginning to contribute significantly around prepulses of −80 mV and gradually decreasing at higher voltages. With respect to $hNa_V1.9$-1.5Ctail$^{p.L811P}$, this causes a significant flattening of the channel availability curve to a slope factor of −23 ± 6.5 ($P < 0.001$) (Fig. 8 and table S15).

The progressive increase in $Na_V1.9$ current during patch-clamp recordings is likely driven by intracellular modulators, which shift activation to more hyperpolarized potentials and stabilize the open state. However, $mNa_V1.9^{p.L799P}$ (fig. S7 and table S16) and $hNa_V1.9$-1.5Ctail$^{p.L811P}$ (fig. S7 and table S17) exhibit virtually no current increase, likely because they already induce a strong gain-of-function phenotype with hyperpolarized activation and elevated persistent

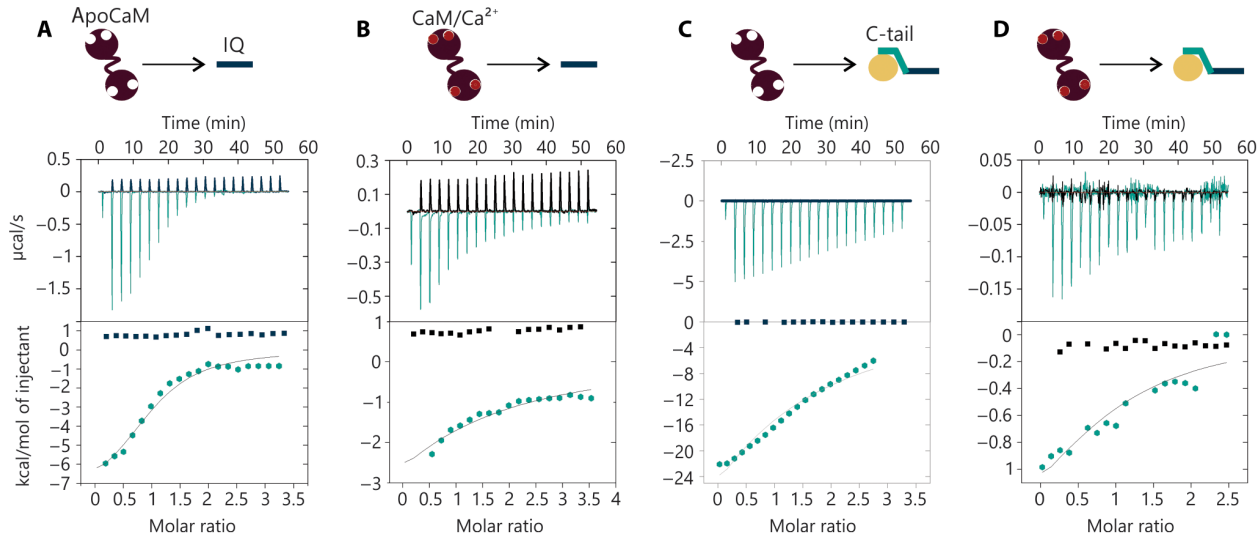

Fig. 7. Investigation of CaM binding to the hNa$_V$1.9 C-tail using ITC. Titration of (**A**) apoCaM (Ca^{2+}-free) into the hNa$_V$1.9 IQ domain (dark blue), (**B**) Ca^{2+}/CaM into the hNa$_V$1.9 IQ domain, (**C**) apoCaM into the hNa$_V$1.9 C-tail, and (**D**) Ca^{2+}/CaM into the Na$_V$1.9 C-tail containing IQ, pre-IQ (teal), and EF-hand (yellow) indicates low affinities that are unlikely to occur under physiological conditions. In titration (D), the heat is low and the binding isotherm is featureless, resulting in a poor fit that again indicates very low affinity. Fitting parameters are shown in table S5.

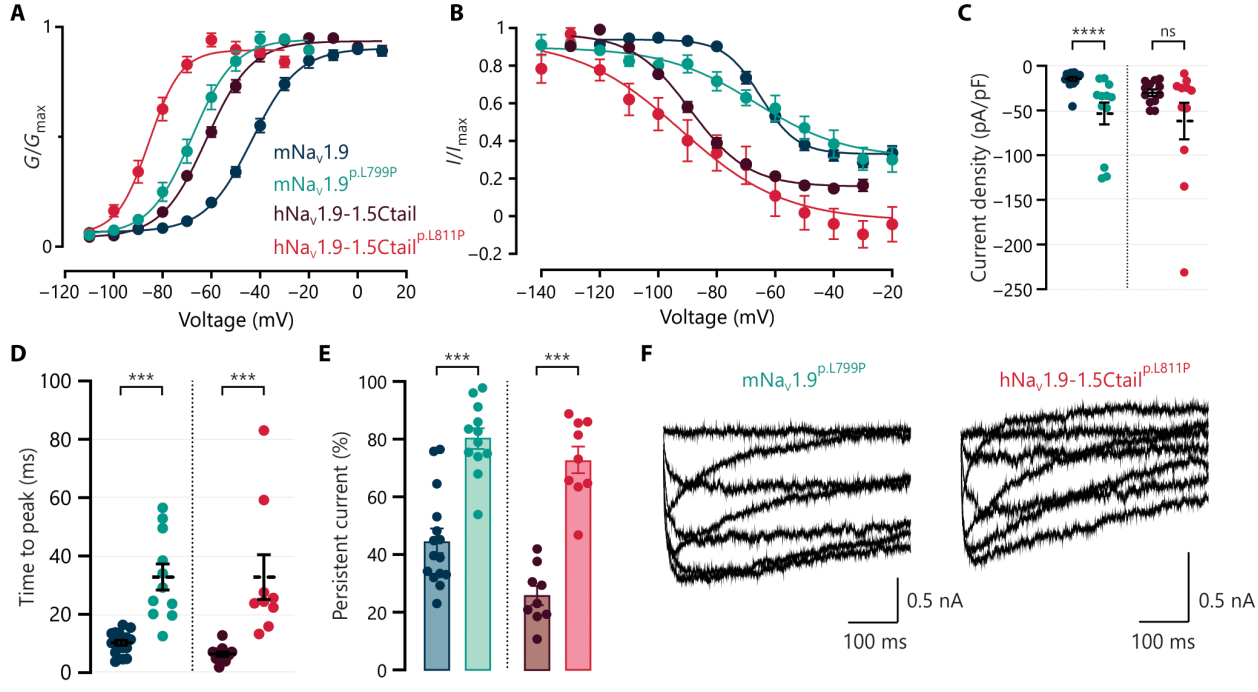

Fig. 8. Characterization of the *p.L811P* (human) and *p.L799P* (mouse) mutations. Mutations were introduced in mNa$_V$1.9 and hNa$_V$1.9-1.5Ctail and transfected into ND7/23 cells. Both mutants demonstrated (**A**) a similar shift in the voltage dependency of activation and (**B**) a distinctive flattening of the channel availability curve. (**C**) Current densities were augmented in both variants, although the difference did not reach statistical significance in hNa$_V$1.9-1.5Ctail$^{p.L811P}$. Kinetics of (**D**) activation and (**E**) fast inactivation were slower for both orthologs. The fraction of persistent current in (E) was measured after 100 ms. As apparent from current traces in (**F**), a 500-ms depolarizing pulse was insufficiently long to achieve full inactivation. An overview of all parameters can be found in tables S14 and S15. ***$P < 0.001$ and ****$P < 0.0001$.

currents, leaving little room for further modulation. Given the lack of high-resolution Na$_V$1.9 structural data, AlphaFold models suggest that both mutations reside in a region critical for gating transitions (DII-S6). Notably, proline substitutions are known to introduce kinks and destabilize α helices, which may affect conformational flexibility and contribute to persistent channel activation.

Overall, these results align with other electrophysiological characterizations of these mutations (*52*, *53*). Recordings from ND7/23 cells transfected with hNa$_V$1.9$^{p.L811P}$ demonstrated a similar deceleration of fast inactivation and a shift in the voltage dependency of activation. Although less pronounced, a change in the slope of the channel availability curve was also observed (*52*). The p.L799P

mutation has only been studied in *SCN11a*$^{+/L799P}$ and *SCN11a*$^{-/L799P}$ mouse DRG, where a detailed characterization can be challenging because of $Na_V1.8$ current interference at higher voltages. Nevertheless, several changes were observed, including slower inactivation, a leftward shift in the half-maximal inactivation voltage, and a flattened channel availability curve. While the overall current density was lower, it was more pronounced at lower voltages. Together, the alignment between our heterologous expression data and prior DRG neuron studies highlights the utility of this system for systematically investigating $Na_V1.9$ mutations and their biophysical contributions to disease.

DISCUSSION

Our understanding of the biophysical properties of $Na_V1.9$ is limited because of challenges in reliably expressing this subtype transiently in heterologous systems (*11*–*14*). Despite the existence of commercially available $Na_V1.9$ stable cell lines, their high cost, limited accessibility, or unsuitability for detailed biophysical investigations through site-directed mutagenesis poses significant drawbacks. In this study, we report a dependable strategy to enhance $mNa_V1.9$ membrane expression to such an extent that robust ionic currents could be measured using a transient expression protocol. Our approach combines multiple elements from the literature including low-temperature incubation of ND7/23 cells and cotransfection of β subunits (*12*–*14*, *24*–*26*, *54*) with new approaches such as the use of a woodchuck hepatitis posttranscriptional regulatory element enhancer in the pcDNA3.4 vector. This element presumably acts at the RNA level without altering the translated protein sequence. Using this strategy, we achieved sufficient current densities of $mNa_V1.9$ for patch-clamp analysis in more than 80% of cells (Fig. 1, Table 1, fig. S2, and table S1). The recorded $mNa_V1.9$-mediated currents exhibited characteristics consistent with existing knowledge on $Na_V1.9$ gating and kinetics (*7*, *13*). As expected, channel activity increased in the presence of GTP-γ-S and in recordings with longer delays after membrane rupture (*18*, *25*, *27*–*30*), possibly due to G protein activation by fluoride ions in the pipette solution (*55*, *56*). Despite using the DRG-derived ND7/23 cell line, significant differences in the voltage dependency of inactivation and kinetics were observed compared to native DRG (Fig. 2 and Table 1), findings that align with the established understanding that ion channel behavior varies across different expression systems. Furthermore, these parameters can exhibit considerable variability between laboratories, influenced by the specific methods used for processing and culturing DRG, patch solutions, voltage protocols, and additional modifications applied to separate $Na_V1.8$- and $Na_V1.9$-mediated currents including the use of intracellular fluoride ions and compounds such as the $Na_V1.8$ inhibitor A-887826 (*22*, *57*–*61*). Variability may also arise from differences in the molecular profile of these cell types, particularly related to which G protein–coupled receptors are expressed (*62*, *63*).

In contrast to $mNa_V1.9$, recording currents from $hNa_V1.9$ proved challenging, potentially due to differences in the amino acid sequence between these orthologs. To identify underlying causes of poor $hNa_V1.9$ expression, we used chimeric constructs incorporating $hNa_V1.5$, a subtype known for its robust expression in various heterologous systems (Figs. 3 to 6, Table 1, and tables S3, S4, and S6 to S13). Substituting the C-tail of $hNa_V1.9$ with that of $hNa_V1.5$ steadily increased current density but only to levels sufficient for patch-clamp recordings in ND7/23 cells when combined with supplementary β subunits and incubation at 28°C. In contrast, $hNa_V1.5$ required none of these conditions. This suggests that the C-tail alone does not fully account for the poor expression of $hNa_V1.9$. Yet, accelerated kinetics and shifts in the channel availability curve were noted, consistent with earlier $Na_V1.9$-based C-tail replacement studies. Previous research with $hNa_V1.9$-$hNa_V1.7$ chimeras identified a 49–amino acid region in the C-tail, encompassing parts of the EF-hand and pre-IQ region, which reduced $hNa_V1.9$ current density (*14*). Our data suggest that the impact of the pre-IQ fragment on current density is limited, implying that the C-terminal part of the EF-hand is, at least in part, a determinant for channel expression levels or trafficking, perhaps in combination with other C-tail regions.

The amino acid sequence of the $Na_V1.9$ C-tail differs substantially from other Na_V channel subtypes, motivating us to explore the ability of this region to confer the distinct inactivation properties of $Na_V1.9$, possibly linked to altered CaM interactions (*41*, *42*, *64*). In addition, distorted CaM binding may also lower open probability, proffering an alternative explanation for the reduction in current density in some of the chimeric channels (*65*). Our ITC experiments uncovered that $Na_V1.9$ can bind both apoCaM and Ca^{2+}/CaM but with a much lower affinity compared to $Na_V1.1$ to $Na_V1.8$, rendering CaM binding unlikely under physiological conditions (Fig. 7). Disrupting CaM binding to Na_V channels has been shown to affect the inactivation process (*42*). However, simply swapping the IQ domain of $Na_V1.9$ into $Na_V1.5$ did not produce any significant gating differences, suggesting that a lack of CaM binding is not the main source of the unique inactivation properties of $Na_V1.9$. Instead, swapping the pre-IQ region, a small segment located between the EF-hand–like and the IQ domain, was sufficient to confer a $Na_V1.9$-like voltage dependency of inactivation. Notably, in the $hNa_V1.9$-$hNa_V1.7$Ctail chimera (*14*), half-maximal inactivation was intermediate between $hNa_V1.9$ and $hNa_V1.7$, supporting our interpretation that the full pre-IQ region is necessary for a complete transformation.

A possible mechanistic explanation for this effect may be found in altered binding of the pre-IQ region to the EF-hand. Previous experiments have shown that the purified EF-hand domain of $Na_V1.5$ can interact with the DIII-DIV linker (*43*, *66*), a cytoplasmic region that connects DIII and DIV of Na_V channels and that contains the IFM-motif that allosterically obstructs Na^+ influx through the pore after channel activation. Mutations in the DIII-DIV linker that disrupt the interaction with the EF-hand domain cause large shifts in channel availability and prevent full inactivation of the channel (*43*). AlphaFold predictions (*67*) of mammalian Na_V channel structures also show a direct interaction between the EF-hand and the DIII-DIV linker (Fig. 9), suggesting that such interactions may occur in states not yet captured by cryo–electron microscopy (cryo-EM) structures of mammalian Na_V channels. In contrast, purified constructs containing both the $Na_V1.5$ EF-hand domain and the pre-IQ region have a ~10-fold reduced affinity for the DIII-DIV linker compared to the EF-hand alone, possibly due to the pre-IQ region and linker occupying the same surface of the EF-hand domain (*39*, *43*). Thus, the stability of pre-IQ interactions with the EF-hand domain may modulate the ability of the latter to bind the DIII-DIV linker, which, in turn, may influence the inactivation process. Additional structural data in different functional states are needed to confirm this hypothesis. It is worth noting that high-resolution structures of $Na_V1.9$ or its fragments are currently unavailable, and cryo-EM structures of other mammalian Na_V

channel subtypes were obtained in the absence of any membrane potential and typically do not display any cryo-EM density for the proximal C-tail, suggesting high mobility under such conditions (*68*–*70*).

$Na_V1.9$ is gaining traction as a potential therapeutic target for sensory perception distortions (*71*–*73*). Thus, the transient expression protocol presented here for $mNa_V1.9$ and an $hNa_V1.9$-$hNa_V1.5$C-tail chimera should be a useful tool to further investigate the atypical gating properties of $Na_V1.9$ via structure-function studies, as demonstrated here (Fig. 8), as well as for drug discovery purposes. Moreover, data gathered from our $Na_V1.9$-$Na_V1.5$ chimeric constructs provided insights into the little understood mechanisms that separate $Na_V1.9$ gating from other Na_V channel isoforms.

MATERIALS AND METHODS

Plasmids and reagents

Mouse *SCN11a* and human *SCN11A* were cloned into a pcDNA3.4 vector (purchased from GenScript). The $hNa_V1.9$-h1.5 chimeras were derived from a pcDNA3.1-based construct (Thermo Fisher Scientific) containing *SCN11A* with sfGFP attached N-terminally and two repeats of a GGGS linker in between. This construct was modified with silent mutations to create unique restriction sites in the loops between domains I, II, III, and IV (DI to DIV) and an additional restriction site in a conserved region of DIV transmembrane segment 6 (S6) to replace the C-tail. For each chimera, one of the five segments flanked by the restriction sites was cut out and swapped with the corresponding part of $hNa_V1.5$ and flanked by the same restriction sites (GenScript). The $hNa_V1.5$-h1.9 constructs were derived from a plasmid containing *SCN5A* cloned into pCMV6-Entry (Origene). Site-directed mutagenesis introduced a silent mutation that created a Hind III restriction site in the same conserved region of DIV S6, and the C-terminal section was substituted with that of $hNa_V1.9$ or the same region of the $hNa_V1.5$ tail containing the $hNa_V1.9$ IQ, pre-IQ, or pre-IQ and EF-hand region. For the mouse β_1 and β_2 subunits, a construct was produced that contained both *SCN1b* and *SCN2b* in the same open reading frame, separated by a T2A self-cleaving peptide.

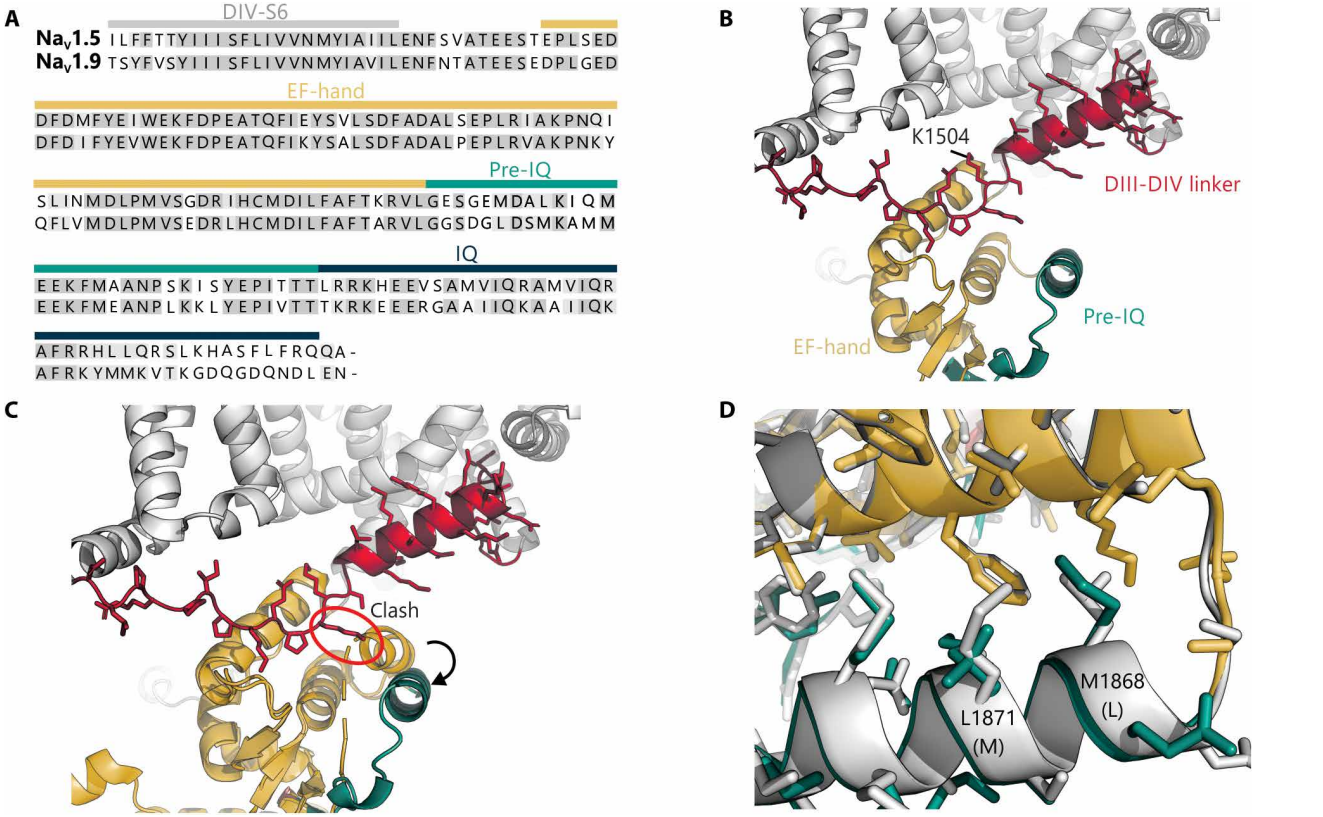

Fig. 9. Overview of targeted regions within the C-tail of $hNa_V1.5$ and $hNa_V1.9$. (**A**) Sequence alignment of $hNa_V1.5$ and $hNa_V1.9$ C-tail regions, starting behind the last segment of domain IV (DIV-S6, gray) and the regions for CaM binding: the EF-hand domain (yellow), pre-IQ (teal), and IQ domain (dark blue). Identical (dark gray) and conserved (light gray) residues are highlighted. (**B**) AlphaFold model of $hNa_V1.5$, showing a close-up around the proximal C terminus. In this model, the linker between DIII and DIV (red) makes several interactions with the EF-hand domain, including a salt bridge that includes K1504 in the DIII-DIV linker. The K1504E/K1505E double mutant was shown to decrease inactivation and to cause a left shift in the steady-state inactivation curve (*43*), suggesting that this interaction is involved in inactivation gating. (**C**) Superposition of the model from (B) with a crystal structure of the $hNa_V1.5$ C-tail that does not include the DIII-DIV linker [PDB (Protein Data Bank) ID: 6MUD; (*39*)]. Here, the pre-IQ domain is at a different location that would clash with the DIII-DIV linker, suggesting that it has to move to allow the interaction of the DIII-DIV linker with the EF-hand domain. This is in agreement with ITC data showing that the affinity of the EF-hand domain for the III-IV linker is weaker when the pre-IQ region is present (*43*). (**D**) Differences in the pre-IQ region at the interface with the EF-hand domain in $hNa_V1.5$ (colors) and $hNa_V1.9$ (white). Shown is a superposition of a crystal structure of the $hNa_V1.5$ C-tail (PDB ID: 6MUD) and a homology-based model of the $hNa_V1.9$ C-tail using the $hNa_V1.5$ C-tail as a template. Among the several pre-IQ domain residues that differ between these isoforms are two residues directly at the interface. The labels indicate $hNa_V1.5$ residues, with the corresponding amino acid residues in $hNa_V1.9$ in between brackets.

Chemicals were purchased from Sigma-Aldrich, and enzymes were purchased from New England Biolabs. TTX and A-887826 were purchased from Tocris.

Cell culture

ND7/23 cells were purchased from Sigma-Aldrich and cultured in Dulbecco's modified Eagle's medium (DMEM; Gibco), supplemented with 10% fetal bovine serum (Gibco), 1% penicillin-streptomycin (Gibco), and 2 mM L-glutamine (Gibco). The medium for HEK293T cells (Sigma-Aldrich) was DMEM/F12 (Gibco) with the same supplements. All cells were kept in an incubator at 37°C and 5% CO_2. When cells were split, Accutase (Thermo Fisher Scientific) was used to suspend HEK293T cells, whereas ND7/23 cells were suspended mechanically. Cells were periodically screened for mycoplasma contamination.

Transfection

Cells were plated the day before transfection and used at a confluence of ~60 to 70%. Transfection was performed using LipoJet (SignaGen), according to the manufacturer's protocol and with a DNA (micrograms)–to–LipoJet reagent (microliters) ratio of 3:1. For all $Na_V1.9$-based constructs, ND7/23 cells were plated in a 24-well plate and transfected with 450 ng of the construct under investigation and 50 ng of a plasmid containing both the mouse β_1 and β_2 subunits. After transfection, the cells were incubated for 24 hours at 37°C before replacing the medium and transferring the cells to an incubator set at 28°C. Cells were used the next day for patch-clamp or immunocytochemistry experiments. $Na_V1.5$-based constructs were expressed in HEK293T cells plated in 12-well plates. The transfection mixture was prepared with 500 ng of the plasmid without additional β subunits or low-temperature incubation, unless stated otherwise. Cells were transfected in the afternoon and incubated overnight at 37°C before use in patch-clamp recordings or lysis for total RNA extraction. For all electrophysiological recordings, 50 ng of a plasmid containing mCherry was cotransfected to allow the identification of transfected cells.

Reverse transcription quantitative polymerase chain reaction

HEK293T cells were transfected with $hNa_V1.5$, $hNa_V1.5$-1.9Ctail, or vehicle (LipoJet only) in triplicate. Cells were suspended the morning after transfection, and RNA was extracted using the Monarch total RNA extraction kit (New England Biolabs). RNA quality and quantity were assessed using spectrophotometry (BioDrop μLite+; Biochrom). To remove residual genomic DNA, 5 μg of RNA was treated with 1 μl of deoxyribonuclease I and purified using the DNA-free Kit (Thermo Fisher Scientific). Next, the LunaScript RT SuperMix Kit (New England Biolabs) was used to generate cDNA from 1 μg of RNA sample according to the manufacturer's guidelines. PCR reactions were assembled using the Luna Universal Probe qPCR Master Mix (New England Biolabs) with 0.2 μl of cDNA. Quantitative PCR reactions were run on the LightCycler 480 (Roche Diagnostics) in triplicate. The primers for SCN5A were designed in Primer3 and had the following sequences: forward, CTTCACCGCCATTTACACCT; reverse, TGCGTAAGGCTG-AGACATTG. Two reference genes were used for normalization: hGAPDH (Origene, cat. no. HP205798) and hACTB (Origene, cat. no. HP204660). The absence of contamination was verified by the inclusion of no-template controls for each primer pair in the experiment. In addition, each cDNA reaction was run in parallel with a reaction without reverse transcriptase (RT; no-RT control). There was at least a 7.8 Ct (threshold cycle) difference between RT and no-RT reactions for all the samples, except the vehicle condition, indicating that most of the cDNA detected originated from RNA, rather than residual transfected cDNA. Analysis was performed according to the ΔΔCt method.

Immunocytochemistry

Glass coverslips (Fisherbrand; Thermo Fisher Scientific) were acid washed in 1 M HCl for 3 days, washed extensively in distilled H_2O, and coated with poly-D-lysine (Gibco) at room temperature for 1 hour. Transfected ND7/23 cells were plated on these coverslips and allowed to attach for 1 to 2 hours before fixation in 4% paraformaldehyde for 15 min. The cells were then permeabilized in 0.2% Triton X-100 for 10 min and blocked with 0.5% fish skin gelatin for 1 hour. Because all $hNa_V1.9$-based constructs have an N-terminal GFP tag, a chicken anti-GFP antibody (Abcam) was used to visualize protein expression. The primary antibody was incubated overnight at 4°C, washed off, and replaced with a secondary antibody for 1 hour at room temperature (goat anti-chicken Alexa Fluor 488, Thermo Fisher Scientific). Both antibodies were diluted 1:1000 in antibody dilution buffer containing 1% bovine serum albumin (Gibco) and 0.025% Triton X-100. Coverslips were mounted in Vectashield with 4′,6-diamidino-2-phenylindole (Vector Laboratories) and visualized on a Nikon Ti epifluorescent microscope with a 20× objective. All digital images were acquired with an exposure time on the fluorescein isothiocyanate filter of 1 s.

Mouse DRG preparation

Glass coverslips were acid washed for 3 days in 1 M HCl, followed by sterilization and storage in 70% ethanol. Before usage, each coverslip was placed in a well of a 24-well plate and washed with sterile distilled H_2O. After drying, the coverslips were coated with poly-D-lysine (50 μg/ml; Gibco) overnight at 4°C. Just before isolation, coverslips were washed again and covered with laminin (10 to 20 μg/ml). C57BL/6J mice aged 8 to 12 weeks (Janvier Labs) were euthanized by cervical dislocation under an approved UGent Animal Ethics Committee protocol (ECD 20-36). The vertebral column was isolated and trimmed of excess muscle tissue and placed in ice-cold Hanks' balanced salt solution (HBSS; Gibco). After bisecting the column, spinal cord tissue was removed and 10 to 15 DRGs were harvested from the thoracolumbar region. Roots of the ganglia were removed before transferring them to a tube of ice-cold HBSS. Ganglia were then dissociated in an enzymatic mixture of dispase (2.5 mg/ml; Gibco) and collagenase type II (1.5 mg/ml; Worthington) dissolved in HBSS. After 45 to 50 min of dissociation at 37°C, the DRGs were allowed to settle and the enzymatic mixture was replaced with 600 μl of DRG medium [DMEM/F12 with 10% fetal bovine serum, 1% penicillin-streptomycin, and GlutaMAX (Gibco)]. Subsequently, the ganglia were gently triturated using fire-polished glass pipettes of decreasing diameters. The resulting cell suspension was centrifuged for 1 min at 100*g* and suspended in 15 μl of DRG medium per coverslip. Next, the laminin on the prepared coverslips was quickly replaced with the cell suspension. The neurons were allowed to attach for 1 hour before flooding the well with culture medium. Recordings were conducted 1 to 10 hours after plating.

Patch-clamp electrophysiology

Fire-polished pipettes were pulled from borosilicate glass (A-M Instruments) to a resistance of 2.0 to 3.5 megohms using a P-1000

puller (Sutter Instruments). Whole-cell voltage-clamp recordings were acquired at room temperature using a MultiClamp 700B amplifier and pClamp10 software (Molecular Devices). The series resistance was compensated for 65 to 85%. The recorded currents were filtered at 10 kHz and sampled at 20 kHz. Leak was subtracted using a -P/4 protocol. For recordings in ND7/23 and HEK293T cells, the extracellular (EC) solution contained 145 mM NaCl, 10 mM Hepes acetic acid, 3 mM KCl, 1.8 mM $CaCl_2$, and 1 mM $MgCl_2$. For $Na_V1.9$ recordings from ND7/23 cells, the intracellular (IC) solution contained 10 mM NaF, 110 mM CsF, 20 mM CsCl, 2 mM EGTA, and 10 mM Hepes acetic acid. The fluoride concentration was lower for $hNa_V1.5$ recordings from HEK293T cells: 100 mM CsCl, 30 mM CsF, 10 mM Hepes acetic acid, and 10 mM EGTA. The osmolarity of all solutions was tuned with glucose to 300 to 305 mosmol, and pH was adjusted to 7.35 with either NaOH (EC) or CsOH (IC). To remove endogenous TTX-sensitive currents, TTX was added to the EC solution, 50 nM for HEK293T cells and 100 nM for ND7/23 cells. Liquid junction potentials were calculated using pClamp 10 as ~8 mV for the ND7/23 solutions and ~6 mV for the HEK293T solutions and were not corrected. For recordings of $hNa_V1.9$ and $hNa_V1.9$-based chimeras, ND7/23 cells were held at −120 mV. The voltage dependency of activation and kinetics were assessed with 100-ms pulses that were increased in 10-mV steps from −110 mV. The voltage dependency of inactivation/channel availability protocol consisted of an incremental 500-ms prepulse starting from −140 mV and going up to +10 mV in 10-mV steps, followed by a 500-ms pulse to −30 mV to open all available (noninactivated) channels. These two protocols were combined into a single protocol for the evaluation of currents from $hNa_V1.5$-based constructs in HEK293T cells. From the holding potential of −100 mV, a 500-ms pulse to a voltage between −140 and +30 mV was applied with an increase of 10 mV per sweep, followed by a 50-ms pulse to −20 mV. Comparisons between constructs were based on recordings between 3 and 6 min after opening. Steady-state protocols were always measured after at least 7 min. For DRG recordings, the EC solution contained 70 mM NaCl, 70 mM choline Cl, 3 mM KCl, 10 mM Hepes acetic acid, 20 mM TEA-Cl, 1 mM $CaCl_2$, and 1 mM $MgCl_2$. The IC solution contained 140 mM CsF, 10 mM NaCl, 10 mM Hepes acetic acid, 2 mM $MgCl_2$, 1 mM EGTA, and 0.1 mM $CdCl_2$. Osmolarity was adjusted to 320 mosmol (EC) and 300 mosmol (IC), and pH was 7.35 for both solutions. To isolate $mNa_V1.9$ currents, 1 μM TTX and 1 μM A-887826 ($Na_V1.8$ blocker) were added to the EC solution. In combination with the use of intracellular F^-, this provides a window of voltages where $Na_V1.9$ currents can be studied without interference of $Na_V1.8$. At hyperpolarized voltages, the distinction between $Na_V1.8$ and $Na_V1.9$ currents is clear. However, at more depolarized voltages, we rely not only on current inhibition by A-887826 but also on the distinct biophysical properties of $Na_V1.9$ currents at room temperature, particularly their significantly slower kinetics compared to $Na_V1.8$. In addition, we avoid drawing conclusions from voltage ranges where $Na_V1.8$ remains active, typically limiting our analysis to voltages around −10 mV and below, where $Na_V1.9$ is fully active, to minimize potential contamination from residual $Na_V1.8$ currents. DRG neurons were held at −90 mV during recordings. The conductance-voltage (*G*-*V*) relationship was recorded in 5-mV steps from −80 mV with a pulse duration of 100 ms. Channel availability was measured at −20 mV after a 500-ms prepulse ranging from −140 to +20 mV. Recordings were started 4 to 6 min after membrane rupture or after 7 to 9 min for channel availability protocols. Current density was normalized to cell capacitance. Reversal potentials (E_{rev}) were estimated using the Nernst equation and used to calculate conductance (*G*) according to the equation $G = I/(V - E_{rev})$. Conductance was normalized to the maximal value. For DRG recordings, the maximum conductance was calculated below −10 mV to avoid contamination with $Na_V1.8$ currents. The voltage error was considered acceptable <10 mV for ND7/23 and HEK293T recordings and <15 mV for DRG recordings. The voltage dependency of activation and steady-state inactivation curves were fitted with the Boltzmann function: $y = 1/[1 + \exp(V_{50} - V_m)/k]$, where V_m is the test potential and *k* is the slope factor. To ensure reliable comparisons of kinetic parameters and persistent currents across constructs, measurements were taken at the voltage that generated the highest current in each individual cell (hereafter referred to as the "peak voltage"). Voltage protocols are visualized in fig. S1.

Purification of CaM and the $hNa_V1.9$ C-tail

Human CaM was expressed as a fusion protein containing a His6-tag and a tobacco etch virus protease site and was expressed and purified as described before (*39*). The human $Na_V1.9$ C-tail (residues 1618 to 1766) was cloned into a modified pET28 vector encoding a His6-tag, maltose binding protein, and a tobacco etch virus protease site, followed by the protein construct (*39*). The construct was expressed in Rosetta(DE3)plysS *Escherichia coli* cells. At an optical density at 600 nm of ~0.6, the temperature was lowered to 18°C and expressed for 15 hours after addition of 250 μM isopropyl-β-D-thiogalactopyranoside. Cells were lysed via sonication in buffer containing 50 mM Hepes (pH 7.4), 250 mM NaCl, 10 mM $CaCl_2$, and 10% sucrose, supplemented with deoxyribonuclease I (25 μg/ml), lysozyme (25 μg/ml), and 400 μM phenylmethylsulfonyl fluoride. After removal of insoluble material by centrifugation at 35,000*g* for 30 min, the supernatant was applied to a His-trap column (Cytiva), washed with buffer A [50 mM Hepes (pH 7.4) and 250 mM NaCl], and eluted with buffer B [buffer A and 500 mM imidazole (pH 7.4)]. The elution fractions were concentrated to 1.5 ml using a 50-kDa-molecular-weight-cutoff (MWCO) concentrator (Amicon) and applied to a prep-grade Sephacryl200 column (Cytiva). Fractions containing the sample were flash frozen in liquid N_2 until ITC experiments.

Isothermal titration calorimetry

All ITC experiments were performed on an ITC200 instrument (Malvern). Both CaM and the $Na_V1.9$ C-tail were dialyzed using a 3.5-kDa-MWCO membrane for at least 24 hours against a buffer containing 25 mM Hepes (pH 7.4), 200 mM KCl, and either 1 mM EGTA or 20 mM $CaCl_2$ to obtain data for Ca^{2+}-free or Ca^{2+}-loaded CaM. For experiments with the individual IQ domain, a synthetic peptide was obtained from LifeTein labs and dialyzed using a 1-kDa-MWCO membrane. Concentrations of CaM and the C-tail were obtained by measuring the absorbance at 280 nm in Edelhoch buffer using the calculated extinction coefficient under these conditions (*47*). For all ITC experiments, CaM was present in the injector, with the IQ or C-tail in the cell, using 20 injections of 2 μl each at 25°C. All ITC data were analyzed in an ITC-specific version of Origin 7.0 (Malvern).

Data analysis

Data were analyzed and visualized using Clampfit11.2 (Molecular Devices), Prism 8 (GraphPad), Fiji (ImageJ), and Office Excel

(Microsoft) and analyzed in the R language with RStudio package (version 2024.04.2+764). All data are represented as the means ± SEM. The choice for a parametric or nonparametric test was motivated by the results of a Shapiro-Wilk test to evaluate normality and Levene's test to assess equal variances for multiple group comparisons. Parametric tests were a two-tailed *t* test or one-way analysis of variance (ANOVA) followed by multiple *t* tests. Nonparametric tests were a Wilcoxon signed-rank test for pairwise comparisons and a Kruskal-Wallis test followed by Dunn's test for multiple comparisons. Data were considered paired for over-time comparisons, and a repeated-measures ANOVA was used if there were more than two time points. *P* values were adjusted using the Hochberg procedure in multiple comparisons and considered significant if $*P < 0.05$, $**P < 0.01$, $***P < 0.001$, and $****P < 0.0001$. Technical replicates are indicated in Figs. 1 to 8 as dot plots and in the provided tables.

Supplementary Materials

This PDF file includes:

Figs. S1 to S8
Tables S1 to S17
References

REFERENCES AND NOTES

1. C. A. Ahern, J. Payandeh, F. Bosmans, B. Chanda, The hitchhiker's guide to the voltage-gated sodium channel galaxy. *J. Gen. Physiol.* **147**, 1–24 (2016).
2. G. Goodwin, S. B. McMahon, The physiological function of different voltage-gated sodium channels in pain. *Nat. Rev. Neurosci.* **22**, 263–274 (2021).
3. W. Brackx, R. de Cássia Collaço, M. Theys, J. V. Cruyssen, F. Bosmans, Understanding the physiological role of NaV1.9: Challenges and opportunities for pain modulation. *Pharmacol. Ther.* **245**, 108416 (2023).
4. S. Dib-Hajj, J. A. Black, T. R. Cummins, S. G. Waxman, NaN/Nav1.9: A sodium channel with unique properties. *Trends Neurosci.* **25**, 253–259 (2002).
5. P. Delmas, B. Coste, Na^+ channel Nav1.9: In search of a gating mechanism. *Trends Neurosci.* **26**, 55–57 (2003).
6. S. D. Dib-Hajj, A. M. Binshtok, T. R. Cummins, M. F. Jarvis, T. Samad, K. Zimmermann, Voltage-gated sodium channels in pain states: Role in pathophysiology and targets for treatment. *Brain Res. Rev.* **60**, 65–83 (2009).
7. T. R. Cummins, S. D. Dib-Hajj, J. A. Black, A. N. Akopian, J. N. Wood, S. G. Waxman, A novel persistent tetrodotoxin-resistant sodium current in SNS-null and wild-type small primary sensory neurons. *J. Neurosci.* **19**, RC43 (1999).
8. J. Huang, C. G. Vanoye, A. Cutts, Y. P. Goldberg, S. D. Dib-Hajj, C. J. Cohen, S. G. Waxman, A. L. George, Sodium channel NaV1.9 mutations associated with insensitivity to pain dampen neuronal excitability. *J. Clin. Invest.* **127**, 2805–2814 (2017).
9. X. Zhang, B. T. Priest, I. Belfer, M. S. Gold, Voltage-gated Na^+ currents in human dorsal root ganglion neurons. *eLife* **6**, e23235 (2017).
10. R. I. Herzog, T. R. Cummins, S. G. Waxman, Persistent TTX-resistant Na^+ current affects resting potential and response to depolarization in simulated spinal sensory neurons. *J. Neurophysiol.* **86**, 1351–1364 (2001).
11. S. N. Bothe, A. Lampert, The insecticide deltamethrin enhances sodium channel slow inactivation of human Nav1.9, Nav1.8 and Nav1.7. *Toxicol. Appl. Pharmacol.* **428**, 115676 (2021).
12. R. O. Goral, E. Leipold, E. Nematian-Ardestani, S. H. Heinemann, Heterologous expression of $Na_V1.9$ chimeras in various cell systems. *Pflugers Arch.* **467**, 2423–2435 (2015).
13. Z. Lin, S. Santos, K. Padilla, D. Printzenhoff, N. A. Castle, Biophysical and pharmacological characterization of Nav1.9 voltage dependent sodium channels stably expressed in HEK-293 cells. *PLOS ONE* **11**, e0161450 (2016).
14. D. V. Sizova, J. Huang, E. J. Akin, M. Estacion, C. Gomis-Perez, S. G. Waxman, S. D. Dib-Hajj, A 49-residue sequence motif in the C terminus of Nav1.9 regulates trafficking of the channel to the plasma membrane. *J. Biol. Chem.* **295**, 1077–1090 (2020).
15. X. Zhou, Z. Xiao, Y. Xu, Y. Zhang, D. Tang, X. Wu, C. Tang, M. Chen, X. Shi, P. Chen, S. Liang, Z. Liu, Electrophysiological and pharmacological analyses of $Na_v1.9$ voltage-gated sodium channel by establishing a heterologous expression system. *Front. Pharmacol.* **8**, 852 (2017).
16. F. Bosmans, M. Puopolo, M.-F. Martin-Eauclaire, B. P. Bean, K. J. Swartz, Functional properties and toxin pharmacology of a dorsal root ganglion sodium channel viewed through its voltage sensors. *J. Gen. Physiol.* **138**, 59–72 (2011).
17. F. Amaya, H. Wang, M. Costigan, A. J. Allchorne, J. P. Hatcher, J. Egerton, T. Stean, V. Morisset, D. Grose, M. J. Gunthorpe, I. P. Chessell, S. Tate, P. J. Green, C. J. Woolf, The voltage-gated sodium channel $Na_v1.9$ is an effector of peripheral inflammatory pain hypersensitivity. *J. Neurosci.* **26**, 12852–12860 (2006).
18. F. Maingret, B. Coste, F. Padilla, N. Clerc, M. Crest, S. M. Korogod, P. Delmas, Inflammatory mediators increase $Na_v1.9$ current and excitability in nociceptors through a coincident detection mechanism. *J. Gen. Physiol.* **131**, 211–225 (2008).
19. F. Touska, B. Turnquist, V. Vlachova, P. W. Reeh, A. Leffler, K. Zimmermann, Heat-resistant action potentials require TTX-resistant sodium channels $Na_V1.8$ and $Na_V1.9$. *J. Gen. Physiol.* **150**, 1125–1144 (2018).
20. H. Maruyama, M. Yamamoto, T. Matsutomi, T. Zheng, Y. Nakata, J. N. Wood, N. Ogata, Electrophysiological characterization of the tetrodotoxin-resistant Na^+ channel, $Na_v1.9$, in mouse dorsal root ganglion neurons. *Pflugers Arch.* **449**, 76–87 (2004).
21. M. F. Jarvis, P. Honore, C.-C. Shieh, M. Chapman, S. Joshi, X.-F. Zhang, M. Kort, W. Carroll, B. Marron, R. Atkinson, J. Thomas, D. Liu, M. Krambis, Y. Liu, S. McGaraughty, K. Chu, R. Roeloffs, C. Zhong, J. P. Mikusa, G. Hernandez, D. Gauvin, C. Wade, C. Zhu, M. Pai, M. Scanio, L. Shi, I. Drizin, R. Gregg, M. Matulenko, A. Hakeem, M. Gross, M. Johnson, K. Marsh, P. K. Wagoner, J. P. Sullivan, C. R. Faltynek, D. S. Krafte, A-803467, a potent and selective $Na_v1.8$ sodium channel blocker, attenuates neuropathic and inflammatory pain in the rat. *Proc. Natl. Acad. Sci. U.S.A.* **104**, 8520–8525 (2007).
22. X.-F. Zhang, C.-C. Shieh, M. L. Chapman, M. A. Matulenko, A. H. Hakeem, R. N. Atkinson, M. E. Kort, B. E. Marron, S. Joshi, P. Honore, C. R. Faltynek, D. S. Krafte, M. F. Jarvis, A-887826 is a structurally novel, potent and voltage-dependent Nav1.8 sodium channel blocker that attenuates neuropathic tactile allodynia in rats. *Neuropharmacology* **59**, 201–207 (2010).
23. B. Coste, N. Osorio, F. Padilla, M. Crest, P. Delmas, Gating and modulation of presumptive $Na_V1.9$ channels in enteric and spinal sensory neurons. *Mol. Cell. Neurosci.* **26**, 123–134 (2004).
24. H. Okuda, A. Noguchi, H. Kobayashi, D. Kondo, K. H. Harada, S. Youssefian, H. Shioi, R. Kabata, Y. Domon, K. Kubota, Y. Kitano, Y. Takayama, T. Hitomi, K. Ohno, Y. Saito, T. Asano, M. Tominaga, T. Takahashi, A. Koizumi, Infantile pain episodes associated with novel Nav1.9 mutations in familial episodic pain syndrome in Japanese families. *PLOS ONE* **11**, e0154827 (2016).
25. C. G. Vanoye, J. D. Kunic, G. R. Ehring, A. L. George, Mechanism of sodium channel $Na_V1.9$ potentiation by G-protein signaling. *J. Gen. Physiol.* **141**, 193–202 (2013).
26. E. Leipold, A. Hanson-Kahn, M. Frick, P. Gong, J. A. Bernstein, M. Voigt, I. Katona, R. O. Goral, J. Altmüller, P. Nürnberg, J. Weis, C. A. Hübner, S. H. Heinemann, I. Kurth, Cold-aggravated pain in humans caused by a hyperactive $Na_V1.9$ channel mutant. *Nat. Commun.* **6**, 10049 (2015).
27. F. Rugiero, M. Mistry, D. Sage, J. A. Black, S. G. Waxman, M. Crest, N. Clerc, P. Delmas, M. Gola, Selective expression of a persistent tetrodotoxin-resistant Na^+ current and Nav1.9 Subunit in myenteric sensory neurons. *J. Neurosci.* **23**, 2715–2725 (2003).
28. R. S. Scroggs, The distribution of low-threshold TTX-resistant Na^+ currents in rat trigeminal ganglion cells. *Neuroscience* **222**, 205–214 (2012).
29. J. A. R. Östman, M. A. Nassar, J. N. Wood, M. D. Baker, GTP up-regulated persistent Na^+ current and enhanced nociceptor excitability require $Na_V1.9$. *J. Physiol.* **586**, 1077–1087 (2008).
30. M. D. Baker, S. Y. Chandra, Y. Ding, S. G. Waxman, J. N. Wood, GTP-induced tetrodotoxin-resistant Na^+ current regulates excitability in mouse and rat small diameter sensory neurones. *J. Physiol.* **548**, 373–382 (2003).
31. K. Y. Sukhanova, A. Koirala, K. S. Elmslie, $Na_V1.9$ current in muscle afferent neurons is enhanced by substances released during muscle activity. *J. Neurophysiol.* **128**, 739–750 (2022).
32. B'SYS GmbH, Swiss Biotech, www.swissbiotech.org/listing/bsys-gmbh/.
33. A. Varró, J. Tomek, N. Nagy, L. Virág, E. Passini, B. Rodriguez, I. Baczkó, Cardiac transmembrane ion channels and action potentials: Cellular physiology and arrhythmogenic behavior. *Physiol. Rev.* **101**, 1083–1176 (2021).
34. D. Jiang, H. Shi, L. Tonggu, T. M. G. El-Din, M. J. Lenaeus, Y. Zhao, C. Yoshioka, N. Zheng, W. A. Catterall, Structure of the cardiac sodium channel. *Cell* **180**, 122–134.e10 (2020).
35. C. Wang, B. C. Chung, H. Yan, S.-Y. Lee, G. S. Pitt, Crystal structure of the ternary complex of a NaV C-terminal domain, a fibroblast growth factor homologous factor, and calmodulin. *Structure* **20**, 1167–1176 (2012).
36. C. Wang, B. C. Chung, H. Yan, H.-G. Wang, S.-Y. Lee, G. S. Pitt, Structural analyses of Ca^{2+}/CaM interaction with NaV channel C-termini reveal mechanisms of calcium-dependent regulation. *Nat. Commun.* **5**, 4896 (2014).
37. S. B. Gabelli, A. Boto, V. H. Kuhns, M. A. Bianchet, F. Farinelli, S. Aripirala, J. Yoder, J. Jakoncic, G. F. Tomaselli, L. M. Amzel, Regulation of the $Na_V1.5$ cytoplasmic domain by calmodulin. *Nat. Commun.* **5**, 5126 (2014).
38. J. B. Yoder, M. Ben-Johny, F. Farinelli, L. Srinivasan, S. R. Shoemaker, G. F. Tomaselli, S. B. Gabelli, L. M. Amzel, Ca^{2+}-dependent regulation of sodium channels $Na_V1.4$ and NaV1.5 is controlled by the post-IQ motif. *Nat. Commun.* **10**, 1514 (2019).
39. B. R. Gardill, R. E. Rivera-Acevedo, C.-C. Tung, F. Van Petegem, Crystal structures of Ca^{2+}–calmodulin bound to Na_V C-terminal regions suggest role for EF-hand domain in binding and inactivation. *Proc. Natl. Acad. Sci. U.S.A.* **116**, 10763–10772 (2019).

40. F. Van Petegem, P. A. Lobo, C. A. Ahern, Seeing the forest through the trees: Towards a unified view on physiological calcium regulation of voltage-gated sodium channels. *Biophys. J.* **103**, 2243–2251 (2012).
41. M. Ben-Johny, P. S. Yang, J. Niu, W. Yang, R. Joshi-Mukherjee, D. T. Yue, Conservation of Ca^{2+}/calmodulin regulation across Na and Ca^{2+} channels. *Cell* **157**, 1657–1670 (2014).
42. P. W. Kang, N. Chakouri, J. Diaz, G. F. Tomaselli, D. T. Yue, M. Ben-Johny, Elementary mechanisms of calmodulin regulation of $Na_V1.5$ producing divergent arrhythmogenic phenotypes. *Proc. Natl. Acad. Sci. U.S.A.* **118**, e2025085118 (2021).
43. B. R. Gardill, R. E. Rivera-Acevedo, C.-C. Tung, M. Okon, L. P. McIntosh, F. Van Petegem, The voltage-gated sodium channel EF-hands form an interaction with the III-IV linker that is disturbed by disease-causing mutations. *Sci. Rep.* **8**, 4483 (2018).
44. W. A. Catterall, Voltage gated sodium and calcium channels: Discovery, structure, function, and pharmacology. *Channels* **17**, 2281714 (2023).
45. S. Noreng, T. Li, J. Payandeh, Structural pharmacology of voltage-gated sodium channels. *J. Mol. Biol.* **433**, 166967 (2021).
46. N. T. Theoharis, B. R. Sorensen, J. Theisen-Toupal, M. A. Shea, The neuronal voltage-dependent sodium channel type II IQ motif lowers the calcium affinity of the C-domain of calmodulin. *Biochemistry* **47**, 112–123 (2008).
47. B. Hille, Ionic channels in nerve membranes, 50 years on. *Prog. Biophys. Mol. Biol.* **169–170**, 12–20 (2022).
48. M. D. Feldkamp, L. Yu, M. A. Shea, Structural and energetic determinants of apo calmodulin binding to the IQ motif of the $Na_V1.2$ voltage-dependent sodium channel. *Structure* **19**, 733–747 (2011).
49. L. Hovey, C. A. Fowler, R. Mahling, Z. Lin, M. S. Miller, D. C. Marx, J. B. Yoder, E. H. Kim, K. M. Tefft, B. C. Waite, M. D. Feldkamp, L. Yu, M. A. Shea, Calcium triggers reversal of calmodulin on nested anti-parallel sites in the IQ motif of the neuronal voltage-dependent sodium channel $Na_V1.2$. *Biophys. Chem.* **224**, 1–19 (2017).
50. B. Chagot, W. J. Chazin, Solution NMR structure of apo-calmodulin in complex with the IQ motif of human cardiac sodium channel NaV1.5. *J. Mol. Biol.* **406**, 106–119 (2011).
51. M. Sarhan, F. V. Petegem, C. A. Ahern, Crystallographic basis for calcium regulation of sodium channels. *Biophys. J.* **102**, 325a (2012).
52. E. Leipold, L. Liebmann, G. C. Korenke, T. Heinrich, S. Gießelmann, J. Baets, M. Ebbinghaus, R. O. Goral, T. Stödberg, J. C. Hennings, M. Bergmann, J. Altmüller, H. Thiele, A. Wetzel, P. Nürnberg, V. Timmerman, P. De Jonghe, R. Blum, H. G. Schaible, J. Weis, S. H. Heinemann, C. A. Hübner, I. Kurth, A de novo gain-of-function mutation in SCN11A causes loss of pain perception. *Nat. Genet.* **45**, 1399–1404 (2013).
53. M. Chen, S. Peng, Z. Xiao, Z. Liu, X. Zhou, Multiple gating processes associated with the distal end of the S6 segment of domain II in the Nav channels. *J. Biol. Chem.* **301**, 108060 (2025).
54. X. Zhou, T. Ma, L. Yang, S. Peng, L. Li, Z. Wang, Z. Xiao, Q. Zhang, L. Wang, Y. Huang, M. Chen, S. Liang, X. Zhang, J. Y. Liu, Z. Liu, Spider venom-derived peptide induces hyperalgesia in $Na_V1.7$ knockout mice by activating Nav1.9 channels. *Nat. Commun.* **11**, 2293 (2020).
55. A. Strunecká, O. Strunecký, J. Patocka, Fluoride plus aluminum: Useful tools in laboratory investigations, but messengers of false information. *Physiol. Res.* **51**, 557–564 (2002).
56. L. Li, The biochemistry and physiology of metallic fluoride: Action, mechanism, and implications. *Crit. Rev. Oral Biol. Med.* **14**, 100–114 (2003).
57. A. M. Rush, S. G. Waxman, PGE_2 increases the tetrodotoxin-resistant $Na_V1.9$ sodium current in mouse DRG neurons via G-proteins. *Brain Res.* **1023**, 264–271 (2004).
58. M. Amsalem, C. Poilbout, G. Ferracci, P. Delmas, F. Padilla, Membrane cholesterol depletion as a trigger of Nav1.9 channel-mediated inflammatory pain. *EMBO J.* **37**, e97349 (2018).
59. J. Qiu, X. Xu, S. Zhang, G. Li, G. Zhang, Modulations of $Na_V1.8$ and $Na_V1.9$ channels in monosodium urate-induced gouty arthritis in mice. *Inflammation* **44**, 1405–1415 (2021).
60. J. Huang, M. Estacion, P. Zhao, F. B. Dib-Hajj, B. Schulman, A. Abicht, I. Kurth, K. Brockmann, S. G. Waxman, S. D. Dib-Hajj, A novel gain-of-function Nav1.9 mutation in a child with episodic pain. *Front. Neurosci.* **13**, 19 (2019).
61. F. Qiu, Y. Li, Q. Fu, Y. Y. Fan, C. Zhu, Y. H. Liu, W. D. Mi, Stromal cell-derived factor 1 increases tetrodotoxin-resistant sodium currents Nav1.8 and Nav1.9 in rat dorsal root ganglion neurons via different mechanisms. *Neurochem. Res.* **41**, 1587–1603 (2016).
62. X. Dong, S. Han, M. J. Zylka, M. I. Simon, D. J. Anderson, A diverse family of GPCRs expressed in specific subsets of nociceptive sensory neurons. *Cell* **106**, 619–632 (2001).
63. P. Ray, A. Torck, L. Quigley, A. Wangzhou, M. Neiman, C. Rao, T. Lam, J.-Y. Kim, T. H. Kim, M. Q. Zhang, G. Dussor, T. J. Price, Comparative transcriptome profiling of the human and mouse dorsal root ganglia: An RNA-seq–based resource for pain and sensory neuroscience research. *Pain* **159**, 1325–1345 (2018).
64. H. Yan, C. Wang, S. O. Marx, G. S. Pitt, Calmodulin limits pathogenic Na+ channel persistent current. *J. Gen. Physiol.* **149**, 277–293 (2017).
65. P. J. Adams, M. Ben-Johny, I. E. Dick, T. Inoue, D. T. Yue, Apocalmodulin itself promotes ion channel opening and Ca^{2+} regulation. *Cell* **159**, 608–622 (2014).
66. H. K. Motoike, H. Liu, I. W. Glaaser, A.-S. Yang, M. Tateyama, R. S. Kass, The Na^+ channel inactivation gate is a molecular complex: A novel role of the COOH-terminal domain. *J. Gen. Physiol.* **123**, 155–165 (2004).
67. J. Jumper, R. Evans, A. Pritzel, T. Green, M. Figurnov, O. Ronneberger, K. Tunyasuvunakool, R. Bates, A. Žídek, A. Potapenko, A. Bridgland, C. Meyer, S. A. A. Kohl, A. J. Ballard, A. Cowie, B. Romera-Paredes, S. Nikolov, R. Jain, J. Adler, T. Back, S. Petersen, D. Reiman, E. Clancy, M. Zielinski, M. Steinegger, M. Pacholska, T. Berghammer, S. Bodenstein, D. Silver, O. Vinyals, A. W. Senior, K. Kavukcuoglu, P. Kohli, D. Hassabis, Highly accurate protein structure prediction with AlphaFold. *Nature* **596**, 583–589 (2021).
68. X. Pan, Z. Li, Q. Zhou, H. Shen, K. Wu, X. Huang, J. Chen, J. Zhang, X. Zhu, J. Lei, W. Xiong, H. Gong, B. Xiao, N. Yan, Structure of the human voltage-gated sodium channel Nav1.4 in complex with β1. *Science* **362**, eaau2486 (2018).
69. X. Pan, Z. Li, X. Jin, Y. Zhao, G. Huang, X. Huang, Z. Shen, Y. Cao, M. Dong, J. Lei, N. Yan, Comparative structural analysis of human $Na_V1.1$ and $Na_V1.5$ reveals mutational hotspots for sodium channelopathies. *Proc. Natl. Acad. Sci. U.S.A.* **118**, e2100066118 (2021).
70. X. Fan, J. Huang, X. Jin, N. Yan, Cryo-EM structure of human voltage-gated sodium channel $Na_V1.6$. *Proc. Natl. Acad. Sci. U.S.A.* **120**, e2220578120 (2023).
71. S. D. Dib-Hajj, J. A. Black, S. G. Waxman, $Na_V1.9$: A sodium channel linked to human pain. *Nat. Rev. Neurosci.* **16**, 511–519 (2015).
72. J. Salvatierra, M. Diaz-Bustamante, J. Meixiong, E. Tierney, X. Dong, F. Bosmans, A disease mutation reveals a role for NaV1.9 in acute itch. *J. Clin. Invest.* **128**, 5434–5447 (2018).
73. D. L. Bennett, A. J. Clark, J. Huang, S. G. Waxman, S. D. Dib-Hajj, The role of voltage-gated sodium channels in pain signaling. *Physiol. Rev.* **99**, 1079–1151 (2019).
74. V. Jäger, K. Büssow, T. Schirrmann, "Transient recombinant protein expression in mammalian cells" in *Animal Cell Culture*, M. Al-Rubeai, Ed. (Springer International Publishing, 2015), pp. 27–64.
75. S. Zou, K. Scarfo, M. H. Nantz, J. G. Hecker, Lipid-mediated delivery of RNA is more efficient than delivery of DNA in non-dividing cells. *Int. J. Pharm.* **389**, 232–243 (2010).
76. I. Vetter, C. Mozar, T. Durek, J. S. Wingerd, P. F. Alewood, M. J. Christie, R. J. Lewis, Characterisation of Nav types endogenously expressed in human SH-SY5Y neuroblastoma cells. *Biochem. Pharmacol.* **83**, 1562–1571 (2012).
77. L. V. Dekker, Z. Daniels, C. Hick, K. Elsegood, S. Bowden, T. Szestak, J. R. Burley, A. Southan, D. Cronk, I. F. James, Analysis of human Nav1.8 expressed in SH-SY5Y neuroblastoma cells. *Eur. J. Pharmacol.* **528**, 52–58 (2005).
78. C. E. P. Goldring, N. R. Kitteringham, R. Jenkins, C. A. Lovatt, L. E. Randle, A. Abdullah, A. Owen, X. Liu, P. J. Butler, D. P. Williams, P. Metcalfe, C. Berens, W. Hillen, B. Foster, A. Simpson, L. McLellan, B. K. Park, Development of a transactivator in hepatoma cells that allows expression of phase I, phase II, and chemical defense genes. *Am. J. Physiol.-Cell Physiol.* **290**, C104–C115 (2006).
79. J. V. O'Mahoney, T. E. Adams, Optimization of experimental variables influencing reporter gene expression in hepatoma cells following calcium phosphate transfection. *DNA Cell Biol.* **13**, 1227–1232 (1994).
80. I. Marten, F. Gaymard, G. Lemaillet, J.-B. Thibaud, H. Sentenac, R. Hedrich, Functional expression of the plant K^+ channel KAT1 in insect cells. *FEBS Lett.* **380**, 229–232 (1996).
81. X. Shen, D. L. Hacker, L. Baldi, F. M. Wurm, Virus-free transient protein production in Sf9 cells. *J. Biotechnol.* **171**, 61–70 (2014).
82. M. Chahine, M. E. O'Leary, Regulatory role of voltage-gated Na^+ channel β subunits in sensory neurons. *Front. Pharmacol.* **2**, 70 (2011).
83. M. L. Milstein, H. Musa, D. P. Balbuena, J. M. B. Anumonwo, D. S. Auerbach, P. B. Furspan, L. Hou, B. Hu, S. M. Schumacher, R. Vaidyanathan, J. R. Martens, J. Jalife, Dynamic reciprocity of sodium and potassium channel expression in a macromolecular complex controls cardiac excitability and arrhythmia. *Proc. Natl. Acad. Sci. U.S.A.* **109**, E2134–E2143 (2012).
84. R. G. Utrilla, P. Nieto-Marín, S. Alfayate, D. Tinaquero, M. Matamoros, M. Pérez-Hernández, S. Sacristán, L. Ondo, R. de Andrés, F. J. Díez-Guerra, J. Tamargo, E. Delpón, R. Caballero, Kir2.1-Nav1.5 channel complexes are differently regulated than Kir2.1 and Nav1.5 channels alone. *Front. Physiol.* **8**, 903 (2017).
85. M. C. M. Franck, A. Stenqvist, L. Li, J. Hao, D. Usoskin, X. Xu, Z. Wiesenfeld-Hallin, P. Ernfors, Essential role of Ret for defining non-peptidergic nociceptor phenotypes and functions in the adult mouse. *Eur. J. Neurosci.* **33**, 1385–1400 (2011).
86. F. Wu, M. Quinonez, M. DiFranco, S. C. Cannon, Stac3 enhances expression of human $Ca_V1.1$ in *Xenopus* oocytes and reveals gating pore currents in HypoPP mutant channels. *J. Gen. Physiol.* **150**, 475–489 (2018).
87. J. Niu, W. Yang, D. T. Yue, T. Inoue, M. Ben-Johny, Duplex signaling by CaM and Stac3 enhances CaV1.1 function and provides insights into congenital myopathy. *J. Gen. Physiol.* **150**, 1145–1161 (2018).
88. A. Kawaguchi, H. Asano, K. Matsushima, T. Wada, S. Yoshida, S. Ichida, Enhancement of sodium current in NG108-15 cells during neural differentiation is mainly due to an increase in NaV1.7 expression. *Neurochem. Res.* **32**, 1469–1475 (2007).
89. R. V. Haberberger, C. Barry, D. Matusica, Immortalized dorsal root ganglion neuron cell lines. *Front. Cell. Neurosci.* **14**, 184 (2020).
90. D. Motlagh, K. J. Alden, B. Russell, J. García, Sodium current modulation by a tubulin/GTP coupled process in rat neonatal cardiac myocytes. *J. Physiol.* **540**, 93–103 (2002).

91. Y.-S. Long, Q.-H. Zhao, T. Su, Y.-L. Cai, Y. Zeng, Y.-W. Shi, Y.-H. Yi, H.-H. Chang, W.-P. Liao, Identification of the promoter region and the 5′-untranslated exons of the human voltage-gated sodium channel Nav1.1 gene (SCN1A) and enhancement of gene expression by the 5′-untranslated exons. *J. Neurosci. Res.* **86**, 3375–3381 (2008).
92. L.-H. Sun, M.-L. Yan, X.-L. Hu, L.-W. Peng, H. Che, Y.-N. Bao, F. Guo, T. Liu, X. Chen, R. Zhang, T. Ban, N. Wang, H.-L. Liu, X. Hou, J. Ai, MicroRNA-9 induces defective trafficking of Nav1.1 and Nav1.2 by targeting Navβ2 protein coding region in rat with chronic brain hypoperfusion. *Mol. Neurodegener.* **10**, 36 (2015).
93. K. H. Asrani, J. D. Farelli, M. R. Stahley, R. L. Miller, C. J. Cheng, R. R. Subramanian, J. M. Brown, Optimization of mRNA untranslated regions for improved expression of therapeutic mRNA. *RNA Biol.* **15**, 756–762 (2018).
94. S.-Y. Wang, K. Bonner, C. Russell, G. K. Wang, Tryptophan scanning of D1S6 and D4S6 C-termini in voltage-gated sodium channels. *Biophys. J.* **85**, 911–920 (2003).
95. P. Subramanyam, D. D. Chang, K. Fang, W. Xie, A. R. Marks, H. M. Colecraft, Manipulating L-type calcium channels in cardiomyocytes using split-intein protein transsplicing. *Proc. Natl. Acad. Sci. U.S.A.* **110**, 15461–15466 (2013).

Acknowledgments
Funding: This work was supported by the following: Research Foundation–Flanders grant G000220N (to F.B.), ERA-NET Neuron grant G0H8120N (to F.B. and F.V.P.), and FWO fundamental research fellowship 1106221N (to M.T.). **Author contributions:** M.T.: writing—original draft, conceptualization, investigation, writing—review and editing, methodology, resources, funding acquisition, formal analysis, and visualization. J.D.W.: investigation and methodology. K.W.: investigation, writing—review and editing, validation, and formal analysis. S.G.: investigation and visualization. F.V.P.: writing—original draft, conceptualization, writing—review and editing, funding acquisition, validation, supervision, project administration, and visualization. F.B.: writing—original draft, conceptualization, investigation, writing—review and editing, methodology, resources, funding acquisition, data curation, validation, supervision, formal analysis, project administration, and visualization. **Competing interests:** The authors declare that they have no competing interests. **Data and materials availability:** All data needed to evaluate the conclusions in the paper are present in the paper and/or the Supplementary Materials. Expression constructs can be provided by F.B.'s pending scientific review and a completed material transfer agreement. Requests for plasmids should be submitted to frank.bosmans@vub.be.

Submitted 18 October 2024
Accepted 22 April 2025
Published 28 May 2025
10.1126/sciadv.adt9799